

Galactic Cepheids with Spitzer: I. Leavitt Law and Colors

M. Marengo^{1,2}, N. R. Evans², P. Barmby^{3,2}, G. Bono^{4,5}, D. L. Welch⁶ and M. Romaniello⁷

ABSTRACT

Classical Cepheid variable stars have been important indicators of extragalactic distance and Galactic evolution for over a century. The *Spitzer* Space Telescope has opened the possibility of extending the study of Cepheids into the mid- and far-infrared, where interstellar extinction is reduced. We have obtained photometry from images of a sample of Galactic Cepheids with the IRAC and MIPS instruments on *Spitzer*. Here we present the first mid-infrared period–luminosity relations for Classical Cepheids in the Galaxy, and the first ever Cepheid period–luminosity relations at 24 and 70 μm . We compare these relations with theoretical predictions, and with period–luminosity relations obtained in recent studies of the Large Magellanic Cloud. We find a significant period–color relation for the [3.6] – [8.0] IRAC color. Other mid-infrared colors for both Cepheids and non-variable supergiants are strongly affected by variable molecular spectral features, in particular deep CO absorption bands. We do not find strong evidence for mid-infrared excess caused by warm (~ 500 K) circumstellar dust. We discuss the possibility that recent detections with near-infrared interferometers of circumstellar shells around δ Cep, ℓ Car, Polaris, Y Oph and RS Pup may be a signature of shocked gas emission in a dust-poor wind associated to pulsation-driven mass loss.

Subject headings: Cepheids — distance scale — infrared: stars — stars: mass loss

¹Dept. of Physics and Astronomy, Iowa State University, Ames, IA 50011

²Harvard-Smithsonian Center for Astrophysics, 60 Garden St., Cambridge, MA 02138

³Dept. of Physics and Astronomy, University of Western Ontario, London, Ontario, N6A 3K7 Canada

⁴Dept. of Physics, Università di Roma Tor Vergata, via della Ricerca Scientifica 1, 00133 Roma, Italy

⁵INAF–Osservatorio Astronomico di Roma, via Frascati 33, 00040 Monte Porzio Catone, Italy

⁶Dept. of Physics and Astronomy, McMaster University, Hamilton, Ontario, L8S 4M1, Canada

⁷European Southern Observatory, Karl-Schwarzschild-Str. 2, 85748 Garching bei Munchen, Germany

1. Introduction

Although it was over 100 years ago that Henrietta Leavitt discovered the Cepheid Period–Luminosity relation (PL, Leavitt 1908), or “Leavitt Law”, few tools in astronomy have such enduring importance. Classical Cepheid variable stars are fundamental calibrators of the extragalactic distance scale and in addition their observed properties are a benchmark for stellar evolution models of intermediate mass stars. It is now widely accepted that distances derived from SN Ia are still significantly influenced by the classical Cepheid calibration: Riess et al. (2005) found a change of 15% in the value of H_0 when only modern, high-quality SN Ia data and HST Cepheids were used. Recent works have extended optical and near-infrared PL and period–color (PC) relations to the mid-infrared (mid-IR), where there is less interstellar extinction, with observations of Large Magellanic Cloud (LMC) Cepheids (Freedman et al. 2008; Ngeow & Kanbur 2008; Ngeow et al. 2009; Madore et al. 2009a) with the *Spitzer* Space Telescope (Werner et al. 2004).

Evolutionary and pulsation properties of intermediate-mass stars in the core He-burning phase, like Cepheids, play a crucial role in several long-standing astrophysical problems. They are transition objects between stellar structures ending up their evolution either as white dwarfs or as core collapse supernovae. Therefore, they are not only the most popular primary distance indicators, but are also crucial to understanding the chemical evolution of stellar systems hosting a substantial fraction of young stars, e.g the Galactic disk and the dwarf irregular galaxies in the Local Group and in the Local Volume ($d \lesssim 10$ Mpc).

Although these objects are fundamental for stellar evolution (Bono et al. 2000; Beaulieu et al. 2001), stellar pulsation (Bono et al. 1999; Marconi et al. 2005), and Galactic chemical evolution models (Pedicelli et al. 2009; Spitoni et al. 2009), current predictions are still hampered by several problems. The most outstanding issue is the “Cepheid mass discrepancy” between pulsation masses of classical Cepheids and their evolutionary masses. Evidence was brought forward more than 30 years ago by Fricke et al. (1972) who found that pulsation masses were from 1.5 to 2 times smaller than the evolutionary masses. This conundrum was partially solved (Moskalik et al. 1992) by the new sets of radiative opacities released by the Opacity Project (Seaton et al. 1994) and by OPAL (Rogers & Iglesias 1992). However, several recent investigations focused on Galactic Cepheids (Bono et al. 2001; Caputo et al. 2005) and Magellanic Cloud Cepheids (Beaulieu et al. 2001; Bono et al. 2002; Keller & Wood 2006) suggest that such a discrepancy still amounts to 10–15%. Measured masses of Galactic binary Cepheids (e.g. Evans et al. 2008) are also smaller than predicted by evolutionary models neglecting core convective overshooting during central hydrogen burning phases.

The relative importance of the main factors affecting Cepheid model mass estimates (extra-mixing, rotation, radiative opacity, mass loss and binarity) is still debated. Even

though commonly used semi-empirical relations (Reimers et al. 1975; DeJager & Nieuwenhuijzen 1997) do not predict enough mass loss to solve the Cepheid mass discrepancy problem, mass loss may indeed be the key culprit among the physical mechanisms suggested to explain the mass discrepancy problem. The semi-empirical mass loss relation derived by Reimers et al. (1975) is clearly inadequate to correctly estimate the mass loss for certain evolutionary phases of giant stars (see e.g. Willson 2000). A plausible increase in the typically adopted Reimers wind free parameter ($0.2 \leq \eta \leq 0.4$) does not account for the entire range in mass covered by cluster horizontal branch (central helium burning) stars (Yong et al. 2000; Castellani et al. 2005; Serenelli & Weiss 2005). There is no good reason why a similar discrepancy should not affect intermediate-mass stars.

Mass loss is often betrayed by the presence of dust shells, detectable as infrared excesses, or by stellar winds which produce blue-shifted absorption dips in the ultraviolet. Empirical estimates of mass loss rates based on infrared (IRAS) and ultraviolet (IUE spectra) observations for a large sample of Galactic Cepheids suggest mass-loss rates ranging from 10^{-10} to $10^{-7} M_{\odot} \text{ yr}^{-1}$ (Deasy 1988). However, evidence for mass loss rates high enough to affect evolution is very rare, and it is not clear that mass loss is a wide-spread phenomenon. McAlary & Welch (1986) used IRAS photometry (Beichman et al. 1985) and found evidence of very cool dust ($T_d \lesssim 50 \text{ K}$) around two classical Cepheids (RS Pup and SU Cas) known to be associated with reflection nebulae. Due to the very large IRAS beamsize (as large as $\sim 5 \text{ arcmin}$), however, it was very difficult to separate local dust emission from “Galactic cirrus” background emission. More recently, K band near-IR interferometric observations (Mérand et al. 2006, 2007; Kervella et al. 2006, 2008, 2009) have detected circumstellar emission around five Classical Cepheids: δ Cep, ℓ Car, Polaris, Y Oph and RS Pup. While the nature of the material responsible for this emission remains mysterious, this is a tantalizing suggestion that mass loss activity may be present around these nearby Cepheids. A similar conclusion was also reached by Neilson et al. (2009), that using OGLE (Optical Gravitational Lensing Experiment; Udalski et al. 1999) and *Spitzer* data for Magellanic Cepheids, found evidence of a wide range of mass loss rates.

To investigate this possibility, we have obtained *Spitzer* observations of a sample of Galactic Classical Cepheids. All stars were observed with both the *Spitzer* Infrared Array Camera (IRAC, Fazio et al. 2004) and the Multiband Infrared Photometer for *Spitzer* (MIPS, Rieke et al. 2004). The aim of the IRAC observations was to characterize Galactic Cepheid colors in the mid-IR, where the emission from the photosphere is still dominant, and search for infrared excess related to warm ($\sim 500 \text{ K}$) circumstellar dust. The MIPS observations were intended to investigate the presence of extended emission from cool ($\lesssim 100 \text{ K}$) dust, taking advantage of the higher angular resolution of *Spitzer* (5 arcsec at $24 \mu\text{m}$). In this paper we present the photometry of our Cepheid sample in the IRAC and MIPS bands,

discussing their PL and period-color (PC) relations. The results of our search for extended emission in IRAC and MIPS images will be presented in a separate paper (Barmby et al. in preparation).

The criteria for our sample selection are laid out in section 2, and the observations are described in section 3. The techniques adopted to measure the source photometry in all IRAC and MIPS bands are discussed in detail in section 4. In section 5 we derive the Leavitt Law and PC relations in the IRAC and MIPS bands, and we compare them with similar relations obtained for the LMC. We study the intrinsic mid-IR colors of Cepheids in section 6, where we set limits on infrared excess at *Spitzer* wavelengths. Our results are discussed in section 7 and summarized in section 8.

2. Sample Selection

Our sample stars are listed in Table 1. They include 29 bright ($K < 5.1$) nearby Cepheids, as well as 3 non-variable supergiants and one red giant added for comparison. The sample was selected to cover a range of several characteristics which may influence mass loss, or enable us to understand it better. Several of the Cepheids are in clusters, three are first-overtone pulsators, and eight are in multiple star systems. The range of periods is about a factor of ten, and several Bump Cepheids ($9 \leq P \leq 12$ days) are included so that we could investigate whether these objects present a peculiar mass loss rate. Our sample includes all 9 Cepheids with measured angular diameters (Nordgren et al. 2000; Lane et al. 2002; Kervella et al. 2004) at the time of the *Spitzer* proposal submission, as well as 5 stars (Polaris, S Mus, W Sgr, V350 Sgr, and FF Aql) with observed masses (Evans et al. 1997, 2006, 2008, 2009; Benedict et al. 2007). V350 Sgr, S Mus, RS Pup, and β Dor are the only Cepheids with $60 \mu\text{m}$ excesses observed by IRAS, so they can be used to check the earlier results. Our sample also includes Y Oph, a long period Cepheid with a surprisingly small amplitude and placid velocity structure (based on line profiles). Its unusual characteristics make it a candidate for an unusual history (either mass loss, coalescence, peculiar chemical composition, evolutionary status).

The stars were also selected for the availability of accurate distance determinations (with the exception of the cluster star V636 Sco whose parallax is very uncertain). For 7 Cepheids we have adopted the HST Fine Guidance Sensor parallaxes measured by Benedict et al. (2007), while we have adopted the Hipparcos distance for Polaris (van Leeuwen et al. 2007). For the other stars we have adopted distances derived with the infrared surface brightness (hereafter IRSB) technique (see e.g. Fouqué & Gieren 1997). While the IRSB method can provide very precise parallaxes when the pulsational velocity and lightcurve of a pulsating

star is known, the conversion between the observable radial velocity v_r into pulsational velocity v_p depends on the so-called projection factor $p = v_p/v_r$. The p -factor, despite its name, does not depend exclusively on the geometry of the star, but also on its physical properties, including the period (see e.g. Nardetto et al. 2007). Several $p(P)$ relations have been proposed, and agreement on which one better describes the true dependence of the p -factor from period is missing (see e.g. Romaniello et al. 2008). Until 2007 several catalogs of Cepheid IRSB distances (Storm et al. 2004; Groenewegen et al. 2004; Barnes et al. 2005 among others) used the relation $p = 1.39 - 0.03 \log P$ (Gieren et al. 1993) characterized by a weak dependence from the period. More recently Nardetto et al. (2007) proposed a new “steeper” relation $p = 1.366 - 0.075 \log P$, which is used in the Fouqué et al. (2007) catalog.

In Table 1 we provide two separate columns for the distance of our targets: the first column mainly lists the “new” distance determination from Fouqué et al. (2007), while the second lists the “old” IRSB distances. In both cases, whenever available, we adopt the Benedict et al. (2007) and van Leeuwen et al. (2007) distances, which are independent from the p -factor. For three stars (DT Cyg, V350 Sgr and U Aql) we could not find their IRSB distance estimated using the “old” $p(P)$ relation. For completeness we derive the “old” distance of these stars (plus V636 Sco) using the method described in Fouqué & Gieren (1997). These distances, and the parameters used to derive them, are listed in Table 2. V and $E(B - V)$ are derived from the Dunlap Observatory Database of Galactic Classical Cepheids (Ferne et al. 1995), K magnitudes from van Leeuwen et al. (2007) or Welch et al. (1984), while R_0 and ΔR_0 from Moskalik & Groynya (2005).

All stars except 3 (DT Cyg, SZ Tau and Polaris) are listed as fundamental mode pulsators, according to Fouqué et al. (2007). FF Aql is here assumed to pulsate in the fundamental mode, as proposed by Benedict et al. (2007), despite having been previously classified as a first overtone Cepheid by Feast & Catchpole (1997).

3. Observations

The observations were executed between July 19, 2006 and October 28, 2007 as part of the *Spitzer* Space Telescope Cycle 3 General Observer program with PID 30666. Each star was observed in IRAC 3.6, 4.5, 5.8 and 8.0 μm and MIPS 24 and 70 μm bands. The MIPS 160 μm band was not used: the known near-infrared leak in this filter would have resulted in strong contamination by starlight.

The IRAC observations were designed to provide, whenever possible, high S/N unsaturated images at all wavelengths well within the linearity regime of the detectors, using the

IRAC subarray mode with 0.02 or 0.4 sec frame times. For targets brighter than $K \sim 2.5$ even the shortest subarray frame time was too long to prevent saturation. For this reason, 6 stars were observed using IRAC full frame stellar mode (frame time of 0.4 sec at 3.6 and 4.5 μm and 2 sec at 5.8 and 8.0 μm), with the intent to produce heavily saturated images suitable for PSF-fitting photometry on high S/N unsaturated “wings” and diffraction spikes. Four other targets were observed in both subarray and full frame stellar mode, to provide photometric cross-calibration between the two modes of observations and to check for linearity. Polaris was not observed with IRAC as part of this program, since archival data obtained during Cycle 1 (*Spitzer* program 19) was available. Each star was dithered on the array in 4 (subarray) or 5 (full frame) positions, using a small scale Gaussian offsets pattern, in order to facilitate transient outlier and bad pixel removals, and produce a better spatial sampling of the images. The total time on source, for each band, was 25.6 sec for the subarray observations. Full frame observations had 2.0 sec (3.6 and 4.5 μm) and 10 sec (5.8 and 8.0 μm) total integration times. The IRAC data were reduced starting from the Basic Calibrated Data (BCDs) generated by the *Spitzer* IRAC pipeline versions S14.4.0 through S16.1.0. Mosaic images with a pixel scale of 0.8627 arcsec/pix for each source in each band were then created using the IRACproc post-BCD software (Schuster, Marengo & Patten 2006).

MIPS observations at both 24 μm and 70 μm were obtained with the Photometry Astronomical Observation Template. The 24 μm observations used 1 cycle of 3 sec frames with the standard 16 point dither pattern. The MIPS 70 μm observations used the default pixel scale and small field size, with 1 to 12 cycles of 3 or 10 sec frames (depending on source and background brightness) with the standard dither pattern. The cluster Cepheids S Nor, U Sgr, and V Cen had slightly different 70 μm observations: 2 adjacent fields of view were observed, to increase the sky coverage to $5 \times 5'$. The total on-source integration times were 48.2 sec at 24 μm and from 37.7 to 1,300.2 sec at 70 μm . The MIPS data, generated by the *Spitzer* pipeline version S16.1, was retrieved from the Archive. No post-processing was performed on most of the data: post-BCD mosaics were used for the 24 μm data and most of the 70 μm data (filtered versions were used). For the three cluster stars (S Nor, SZ Tau, U Sgr), the 70 μm data was remosaiced using MOPEX to combine the data for the two fields of view. The pipeline mosaics for two other stars (RS Pup, GH Lup) showed negative sidelobes; for these stars the BCDs were time- and column filtered and the mosaics re-made.

4. Source Photometry

We measured the IRAC Vega magnitude of all sources observed in subarray mode using aperture photometry. We derived photometric zero points from the IRAC absolute calibra-

tion factors (FLUXCONV) in the BCD headers (listed in Table 3). For most sources we used an aperture of 12.2 arcsec radius (~ 10 pixels in the IRAC array pixel scale) with background level determined from a sky annulus with 12.2 and 24.4 arcsec inner and outer radii. This aperture is the standard used for the IRAC point source calibration, and as such corresponds to an aperture correction equal to one. Three stars (AQ Pup, VY Car and FF Aql, see Figure 1) had one or more background sources falling within this aperture, and required using a smaller 6.1 arcsec radius aperture (~ 5 IRAC pixels). For these sources we derived our own aperture corrections, listed in Table 3, using the other stars as templates. This determination of the aperture correction is more reliable than using the values listed in the IRAC Data Handbook¹ (2006), which were obtained from images with different spatial sampling and dither pattern. We have corrected our subarray point source photometry for the position-dependent geometric and gain distortion factors provided by Hora et al. (2008). These factors (f_{corr}) are listed in Table 3 for the subarray central position. The photometric uncertainty was estimated adding in quadrature the sky RMS variation and source photon noise. At 3.6 and 4.5 μm , an extra 1% uncertainty due to uncharacterized pixel-phase variations was also added (see the IRAC Data Handbook, 2006, p. 50).

The IRAC photometry of the stars observed in full frame stellar mode was obtained by fitting the unsaturated “wings” and diffraction spikes of the mosaic images with the IRAC extended Pixel Response Function (PRF). The extended PRF was constructed from multi-epoch deep images of Sirius, Vega (2 epochs), Fomalhaut (2 epochs), ϵ Eridani (2 epochs) and ϵ Indi, obtained in a separate Guaranteed Time Observation program (PID 90) and IRAC calibration observations. The individual observations were reduced with IRACproc, and the mosaic of each star was masked to remove any pixel closer than 50% or 80% to the saturation level to preserve flux linearity. The individual images were then rescaled to one of the images of Vega and combined with a sigma-clipping algorithm in order to remove background sources. The final product is a high S/N representation of the extended features of the IRAC Point Spread Function (PSF) projected on the IRAC pixel grid (e.g. a PRF), and is ideally suited to derive PSF fitting photometry of bright saturated sources. Given that the PRF is normalized as a calibrated image of Vega, the best-fit scaling factor between a star image and the PRF is equal to the flux ratio of the star with Vega, and can be directly converted into Vega magnitudes without relying on the IRAC absolute calibration. Magnitudes derived with this procedure are not affected by the position-dependent geometric and gain distortion factors, since the sources and the PSF stars have all been observed at the center of the IRAC arrays. An image of the IRAC PRF obtained with a similar procedure is shown in Marengo et al. (2009a), and the PRF files are available at the Spitzer Science

¹<http://ssc.spitzer.caltech.edu/irac/dh/>

Center web site².

The photometric error was estimated by bracketing the best subtraction with an over- and under-subtracted fit in which the PSF-subtraction residuals were of the same magnitude as the background noise. The fit was done using only the overlapping region where both the objects in our programs and the PRF were not saturated. This region is relatively narrow (width of $\sim 20 - 30$ pixels) at 3.6 and 4.5 μm , due to the short total exposure time (2 sec) in these two bands. As a consequence, The PSF-fitting photometric errors tend to be larger at 3.6 and 4.5 μm than at 5.8 and 8.0 μm . The dominant source of uncertainty for the PSF-fitting photometry is the “sampling noise” (grid pattern due to the coarse sampling of the IRAC PSF on the pixel grid) in the subtraction residuals. This coherent noise does not follow Poisson statistics. For this reason the photometric errors estimated for the PSF-fitting photometry should not be taken as 1σ statistical errors (as in the case of the aperture photometry uncertainties), but rather as upper and lower limits in the photometric measurements.

To test the agreement between aperture and PSF-fitting photometry we used the 4 stars observed in both modes. In general, the full frame and subarray mode observations of these stars have been executed at different epochs. As a consequence, based on Large Magellanic Cloud (LMC) Cepheid photometry by Madore et al. (2009b), we should expect a variability in the IRAC bands as large as ± 0.4 mag. Still, we can use these stars observed in both modes to assess the cross calibration of the aperture and PSF-fitting methods, although with this limitation. Table 4 and Figure 2 show that we do not measure in our data any statistically significant shift between the subarray and the full frame photometry: the average difference between subarray and full frame magnitudes is much smaller than its RMS variation. The RMS variation (0.02, 0.07, 0.05 and 0.02 mags at 3.6, 4.5, 5.8 and 8.0 μm respectively) is smaller than the average uncertainty in the PSF-fitting photometry estimated with the fit-bracketing method. For V Cen (the only case in which both subarray and full frame observations were executed at the same epoch), the difference between the aperture and PSF fitting photometry is 0.01, -0.04 , -0.02 and -0.02 mags at 3.6, 4.5, 5.8 and 8.0 μm respectively. This is within the uncertainty of the PSF fitting photometry of this star (0.27, 0.16, 0.09 and 0.06 mags, respectively). At least in the case of V Cen, this test can be viewed as an independent confirmation of the IRAC absolute photometric calibration, since aperture photometry depends on the FLUXCONV parameters, while PSF-fitting with our PRF does not.

Table 5 shows the final magnitudes of all sources. When available, we list the IRAC

²<http://ssc.spitzer.caltech.edu/irac/psf.html>

aperture photometry of unsaturated images (which has smaller nominal uncertainty) rather than the PSF-fitting photometry. The PSF-fitting photometry is instead listed for the sources observed only in IRAC full frame mode.

Measurements of MIPS 24 μm flux densities followed standard procedures. Flux densities for most objects were measured in a 20'' radius apertures with background subtraction from sky annuli of 40''–50'' and the recommended aperture correction of 1.13 applied. There are a few stars with apparent extended emission nearby; for these, flux densities were measured in 7'' radius apertures with the same sky annulus, and an aperture correction of 1.61. The flux densities measured for Polaris and ℓ Car (~ 3.7 Jy) are formally above the saturation limit for 3 second exposures, but both objects are below the “hard” saturation limit (4.1 Jy): the pipeline correctly replaced the saturated pixels with values from the 0.5 second exposures taken as part of the photometry AOR. Uncertainties for the 24 μm flux densities were computed using the standard IRAF/PHOT formula as:

$$\sigma^2 = (F/G + A\sigma^2 + A^2\sigma^2/A')^{1/2} \quad (1)$$

where F is the flux in image units (MJy sr^{-1}), G is the effective gain (the product of the detector gain, individual frame exposure time, and number of frames, divided by the FLUXCONV factor which converts from DN s^{-1} to MJy sr^{-1}), A is the aperture area, A' is the background annulus area, and σ is the standard deviation of image counts in the background area. The values listed in Table 5 do not include the 2% uncertainty in the absolute calibration (Engelbracht et al. 2007), the dominant systematic error for these bright stars.

Measurements of MIPS 70 μm flux densities also followed standard procedures. Flux densities were measured in 16'' radius apertures fixed on the 24 μm position, with sky annuli of 18''–39'', and an aperture correction of 2.04. There were no saturation issues in the 70 μm data. Uncertainties in the 70 μm flux densities were calculated using a similar equation to that for MIPS-24, except that for 70 μm data Poisson noise is negligible. Following Carpenter et al. (2008), the uncertainties are increased by extra multiplicative factors of $\eta_{\text{corr}} = 2.5$ (noise correlation between pixels due to re-sampling during mosaicing), and $\eta_{\text{sky}} = 1.5$ (excess sky noise due to the data-taking procedure). The absolute calibration uncertainty at 70 μm is 5% (Gordon et al. 2007), again not included in the data table. A number of stars were not detected at 70 μm : for these sources 3σ upper limits are recorded.

Determining the effects of interstellar extinction on *Spitzer* IRAC and MIPS photometry is tricky, because of the difficulty of estimating the reddening in the Galaxy, compared to that for an external galaxy. Measurements of the Galactic extinction curve (Lutz et al.

1996; Indebetouw et al. 2005; Flaherty et al. 2007; Román-Zúñiga et al. 2007) when scaled to IRAC wavelengths give $A_{5.8\mu m}/A_B \approx 0.04$ (Rieke & Lebofsky 1985; Freedman et al. 2008). We should thus expect reddening at mid-IR wavelengths for all our nearby Cepheids to be negligible, and for this reason we do not correct our data for reddening.

5. Leavitt Law and Period-Color Relations

The advantages of deriving a PL relation (the Leavitt Law) in the mid-IR (rather than in the optical or near-IR) are manifold: luminosity variation amplitudes, metallicity effects and interstellar extinction are all expected to be smaller at longer wavelengths. A well calibrated PL relation in the IRAC and MIPS bands is of great utility for the available Galactic and extragalactic stellar photometric catalogs obtained in the *Spitzer* legacy projects.

The PC relation at optical wavelength provides important diagnostics for basic stellar parameters such as effective temperature and metallicity (see e.g. Sandage et al. 2004, 2009; Tammann et al. 2003 for a comparative study of the PC relations between the Galaxy, the LMC and the SMC). Extending the study of PC relations into the mid-IR offers the chance to study the effects of these parameters on different spectral features, at wavelengths where the interstellar reddening is less important. A firm understanding of the “intrinsic” color properties of classical Cepheids, and their dependence on stellar parameters and period, is also essential to search for the presence of “extrinsic” color excess that may be related to circumstellar dust emission.

5.1. PL Relations

An IRAC PL relation has already been obtained for Cepheids in the LMC (Freedman et al. 2008; Ngeow & Kanbur 2008; Ngeow et al. 2009; Madore et al. 2009a), using data from the SAGE project (Meixner et al. 2006), and was used to derive the distance modulus for two galaxies in the Local Group, NGC 6822 (Madore et al. 2009b) and IC 1613 (Freedman et al. 2009). Using our photometry in Table 5 we can derive the same relation for a sample of Cepheids in our Galaxy. These are the same Cepheids that, by virtue of their independent distance determination, are at the base of the PL relation zero-point calibration.

We derived the best-fit PL relations for all IRAC and MIPS data with a linear least square fit method, weighed on the uncertainty of each photometric point. For IRAC subarray data we use as weight the 3σ photometric uncertainty, while for all other measurements we use the uncertainty quoted in Table 5. In particular, for IRAC full frame photometry we

use the PSF-fit “bracketing” interval, which is similar to a 3σ uncertainty. For MIPS $70\ \mu\text{m}$ data we exclude data points for which only an upper flux limit is available. Table 6 lists the coefficients of the best-fit relations, in the form:

$$M = \alpha [\log P - 1.0] + \beta \quad (2)$$

Note how the PL relations we have derived are based on single epoch measurements, and not on mean photometry that would have required multiple epoch observations. To include the first overtone Cepheids (DT Cyg, SZ Tau and Polaris) in the fit, we have converted their observed period P_1 into a “fundamentalized” period P_0 using the relation:

$$P_1/P_0 = 0.716 - 0.027 \log P_1 \quad (3)$$

from Feast & Catchpole (1997), derived in turn from Alcock et al. (1995). We provide the best-fit PL relations for three different cases. First, using the “new” IRSB distance determination relying on the “steep” $p(P)$ relation. Then, using only the stars for which the astrometric Benedict et al. (2007) and van Leeuwen et al. (2007) distances are available. Last, using the “old” distances based on the $p(P)$ relation with weak period dependence. Note that in both “old” and “new” cases we still use the astrometric distances when available. The best-fit PL relations for the “new” (solid lines) and astrometric (dashed lines) distances are shown in Figure 3.

Table 6 also includes the K band relations from Fouqué et al. (2007), Benedict et al. (2007) and Storm et al. (2004) for the “new,” astrometric, and “old” distances respectively. The table shows that the slopes and zero points of the three cases are consistent within their uncertainties. The astrometric PL relations have larger uncertainties because most of the stars in that sample have the less precise full frame PSF-fitting photometry, and because of the smaller size of the sample. We can however note some trends: the astrometric Leavitt laws are consistently less steep than the relations using IRSB distances. The “old” distances produce steeper relations than the “new” distances. A similar trend is present in the K band relations. The zero points are very similar for all cases, well within their uncertainties.

Figure 3 also shows that FF Aql (data-point at $\log P = 0.73$) closely matches the general trend. If instead, as suggested by Feast & Catchpole (1997), the source was pulsating in the first overtone, its “fundamentalized” PL ratio would be a significant outlier. This result supports the view that FF Aql is indeed behaving as a fundamental mode pulsator as suggested by Benedict et al. (2007).

The dispersion around the best-fit PL relations is ~ 0.2 mag in the four IRAC bands

and MIPS 24 μm , and ~ 0.4 mag at 70 μm . This is comparable with the expected dispersion at *Spitzer* wavelengths, once our photometric and distance uncertainty is taken into account. The larger uncertainty in the best-fit parameters at 70 μm is due to the larger photometric errors and the smaller number of sources for which a measured flux is available at this wavelength.

The dispersion around the best-fit PL relations has correlated and uncorrelated components between bands. The correlated scatter is a consequence of Cepheid variability. The uncorrelated scatter σ_{Δ} is instead due in part to the absolute magnitude uncertainties (geometric sum of the photometric error and the uncertainty in the distance) and in part to intrinsic variations related to the “width” of the Cepheid instability strip (due to differences in metallicity and other stellar parameters). Figure 4 (left column) shows that the correlated component of the fit residual has an amplitude of about -0.3 to $+0.5$ mag. We may assume this value to approximate the amplitude of the Cepheid light curves in the IRAC bands. While the weighted average residual is zero (by virtue of the least-square fit used to derive the PL relation), it is interesting to note that the IRAC residuals are asymmetrically distributed. This may be a reflection of a prevalence of asymmetric light curves in our sample. While the amplitude of the correlated component of the PL dispersion in our data is similar to the one measured in the LMC by Freedman et al. (2008), they do not note any asymmetry in their sample (three times larger). Comparison between our measured σ_{Δ} (~ 0.04 – 0.05) and the absolute magnitude uncertainty (on average ~ 0.15 mag) shows that we do not have enough accuracy to measure the intrinsic scatter in the PL relation, and all the observed scatter can be explained by the uncertainty of our data.

Our sample does not show any correlation between variability and color residuals in the IRAC bands (Figure 4, right column), similar to the result obtained by Madore et al. (2009a) in the LMC. Again, we cannot test for color correlation between the IRAC and MIPS bands due to the different epochs at which the two sets of data were acquired.

5.2. PC Relations

Figure 5 shows the period vs. *Spitzer* color trends in our data. These diagrams are better suited to analyze color variations between the sample Cepheids than the color residuals in Figure 4, because they do not suffer from the larger uncertainties due to the distance estimates necessary to derive the PL fits. Even in the case of colors using only IRAC bands (taken simultaneously, and hence with each star at a given phase), the data show a scatter that is well above the photometric error. The only exception is the $[3.6] - [8.0]$ color, for which it is possible to derive a weighted, least-square best-fit PC relation:

$$[3.6] - [8.0] = 0.039 [\log(P) - 1.0] [\pm 0.008] - 0.019 [\pm 0.011] \quad (4)$$

The only apparent outliers are some nearby Cepheids observed in full frame mode that have large photometric errors, and in particular Polaris which is consistently red in all IRAC colors by ~ 0.1 mag. This detection is above the PSF-fitting photometry uncertainty for this source, but should be taken with care, given that this observation was not planned to maximize the accuracy of the PSF fit, and may suffer from uncharacterized systematic errors. The large scatter in the $[3.6] - [4.5]$ and $[3.6] - [5.8]$ color (as large as ~ 0.1 mag) prevents the determination of a meaningful PC relation in these colors. This scatter (which tends to be larger for long period Cepheids) may be related to either some intrinsic property of the stellar emission (the presence of broad spectral features in their mid-IR spectrum) or some external cause (emission/absorption features of interstellar or circumstellar origin). These two possibilities will be examined in detail in the next section.

Colors combining IRAC and MIPS bands have an additional scatter due to the different epochs at which the data were acquired. We can estimate this scatter to be at least ± 0.4 mag, as determined in the previous section for the IRAC bands (assuming that the variability at MIPS wavelengths is negligible, which is not necessarily the case). To be detected, any excess in the $[3.6] - [24]$ and $[3.6] - [70]$ colors (or other combinations mixing IRAC and MIPS bands) must be larger than 0.4 mag. Figure 5 shows that none of our sources have excess in the $[3.6] - [24]$ color above this threshold (dashed line). None of the sources with a $70 \mu\text{m}$ measured flux has a $[3.6] - [70]$ excess above 3σ of the minimum expected variability scatter (dotted line), with only sources undetected at $70 \mu\text{m}$ above that line. Similar results are obtained by combining the MIPS 24 and $70 \mu\text{m}$ bands with the other IRAC channels.

The $[24] - [70]$ color does not suffer from multi-epoch scatter, but the lack of good photometric measurements for the $70 \mu\text{m}$ band prevent us from determining reliable colors for most of the sources. Only one target (SZ Tau) has a non-zero $[24] - [70]$ color at more than 3σ significance, which may indicate the presence of a true color excess from this star. The significance of this detection will be described in the next paper of this series (Barnby et al., in preparation).

6. Cepheid Mid-IR Colors and Search for Infrared Excess

Dusty mass loss in the wind of a Cepheid star would reveal itself in the form of an infrared excess caused by thermal radiation from the dust grains. IRAC and MIPS are particularly sensitive to this excess, as shown in the case of Asymptotic Giant Branch (AGB)

stars (Marengo et al. 2008). To isolate any excess from our data, we need however to first characterize the intrinsic colors of Cepheids at mid-IR bands. While a systematic study of the infrared spectral properties of Classical Cepheids is beyond the scope of this work, we can use available models of the 10 d period Cepheid ζ Gem (one of our target stars) computed by Marengo et al. (2002) as a test case.

Marengo et al. (2002) developed a method to derive time-dependent hydrodynamic models of classical Cepheids by solving Local Thermodynamical Equilibrium (LTE) plane parallel radiative transfer for a dynamic stellar atmosphere. The dynamic atmosphere, computed in spherical geometry and in non-LTE conditions, was in turn driven by a “pulsation piston” reproducing the correct radial profile of the star. While this procedure was not simultaneously solving the hydrodynamic and radiative transfer solution for the star, it was still able to produce realistic time-dependent intensity spectra, then used to evaluate the temporal variations of the stellar limb darkening at optical and infrared wavelengths (Marengo et al. 2003). The method was applied to the case of ζ Gem to estimate the effect of limb darkening variations on the star’s distance determination with the geometric Baade-Wesselink method (Marengo et al. 2004).

Figure 6 shows the hydrodynamic model spectra of ζ Gem at 5 significant phases: $\phi_L = 0$ (maximum visible luminosity), $\phi_L = 0.32$ (maximum radius), $\phi_L = 0.49$ (minimum visible luminosity), $\phi_L = 0.63$ (a phase at which a shock-wave is crossing the photosphere), $\phi_L = 0.74$ (minimum radius) and $\phi_L = 0.85$ (the phase at which the star was observed with IRAC). The thick line shows the hydrodynamic model spectra, while the thin line shows an equivalent hydrostatic equilibrium atmosphere having the same T_{eff} and $\log g$ of the dynamic models. The two sets of spectra are compared with Rayleigh-Jeans black bodies normalized to the model spectral emission for $\lambda \gtrsim 8 \mu\text{m}$.

It is apparent from the plot that the model spectra of ζ Gem strongly depart from black body spectra at IRAC wavelengths: we should thus expect IRAC colors that are significantly different from zero magnitudes. The second most obvious characteristic of the models is the presence of a broad spectral feature between 4 and 6 μm , due to CO molecular absorption. This feature falls within the band-passes of the IRAC 4.5 and 5.8 μm filters, and is strong enough to have a significant effect on the IRAC colors including these bands. This feature is present in both the dynamic and static models, and is thus a general property of stars with the temperature and gravity of Cepheids, rather than being a consequence of the pulsations. The strength of the feature appears however to be variable with phase: it is stronger when the stellar atmosphere is more expanded, as at maximum radius. When the atmosphere is compressed (as at minimum radius, or when a shock-wave is crossing the photosphere in the dynamic models), the feature is reduced to a minimum. The absorption is also generally

stronger in the static than in the dynamic model spectra (the former corresponding to an atmosphere with a more “relaxed” structure, as opposed to the “compressed” atmosphere in the dynamic models). This is not the only difference between the static and dynamic models: at $\phi_L = 0.63$ (when a shock-wave is transiting in the continuum-forming photosphere) the dynamic and static atmospheres have very different continuum slopes in their spectral emission, reflecting the dramatic consequences of the pulsations in the affecting the structure of the Cepheid atmosphere.

The presence of this CO absorption, and of the time-dependent hydrodynamic effects, induce significant color variations in the IRAC bands. Figure 7 shows the synthetic IRAC colors of the ζ Gem dynamic and static models. The largest spread is in the $[3.6] - [4.5]$ color (~ 0.8 mag and ~ 1 mag in the dynamic and static model respectively), while the $[3.6] - [8.0]$ color shows a much smaller variation (~ 0.08 mag and ~ 0.02 mag). The reason for this difference is that the $[3.6] - [4.5]$ color is affected by the variable CO absorption, while the $[3.6]$ and $[8.0]$ bands are outside this spectral feature. The dynamic model colors in fact are confined for most phases in a smaller region (~ 0.03 mag in both colors), with the exception of a large excursion when the shock-wave crossing the ζ Gem photosphere at $\phi_L = 0.63$ suddenly expands the atmosphere. The $[3.6] - [4.5]$ colors of the static models have instead a large variation that follows closely the changes in the effective temperature of the star.

The figure also shows the actual colors of ζ Gem as observed with IRAC. Due to the large uncertainty of this star’s photometry, the measured colors cannot be used to assess the respective accuracy of the two class of models (the measurement is within 1σ of both model colors at the observation’s phase $\phi_L = 0.85$).

Figure 8 shows the IRAC and MIPS color-color diagrams of the program stars (including the 3 non-variable supergiants and 1 red giant added to the sample for comparison). The dashed and dotted boxes indicate the location of the dynamic and static model IRAC colors. It is clear that the color variation of the ζ Gem models are sufficient to explain the color spread present for most of the program stars. The dynamic models are actually closer in both axes to the actual colors of the observed stars, while the static models seem to have a systematic offset of ~ 0.04 mag in the $[3.6] - [8.0]$ color (the stars appear to be bluer). While it is unwise to extract general considerations from this effect (the color difference is barely significant given the photometric uncertainty, and the models are specific to only one of the stars), this discrepancy suggests that the color effects induced by the dynamics of the Cepheid pulsations may be important in determining their actual IRAC colors. Three stars have a $[3.6] - [4.5]$ colors ($\lesssim -0.15$) significantly different from the range predicted by both the dynamic and static models. These stars are among the longest period Cepheids in

our sample. This suggest that long period Cepheids may present a deeper CO absorption, at least at some pulsation phases, than ζ Gem. Shorter period Cepheids instead show small [3.6] – [4.5] color scatter, suggesting less variability in the CO feature. Polaris shows ~ 0.1 mag redder colors than all other sources or models, but this needs to be confirmed with higher precision photometry for this star.

The colors of the 4 non-variable control stars are indistinguishable from the colors of the Cepheids, confirming that the mid-IR CO spectral feature that is responsible for the color shift is common in giant stars with this spectral type even when not on the Cepheid instability strip.

The comparison of the observed IRAC colors with the ζ Gem models spectra indicates that the [3.6] – [4.5] and [3.6] – [5.8] scatter in the PC plots in Figure 5 is intrinsic. The [3.6] – [8.0] colors are consistent with the model colors. We therefore conclude that there is no measurable extrinsic infrared excess in the IRAC bands, with only the possible exception of Polaris. Given that [3.6] – [8.0] excess would correspond to the presence of warm dust ($T_d \sim 500$ K), this means that we do not find compelling evidence, for most sources, of circumstellar *dusty* wind that could be associated with currently active *dusty* mass loss (contrary to what was stated in Marengo et al. 2009b where Cepheid intrinsic color variations were not taken into account). This result does not exclude however the presence of winds with low dust content.

The [24] – [70] color does not suffer from variability-induced scatter, but the lack of good photometric measurements for the 70 μm band prevents determining reliable colors for most of the sources. The plot shows a trend in this color for the stars in the sample, but this trend is most likely a consequence of having only upper limits for the 70 μm brightness of most stars. Only one star (again SZ Tau) has a [24] – [70] excess above its 3σ photometric error, which may indicate the presence of cold dust ($T_d \sim 50$ K) in the proximity of the star.

7. Discussion

The reliability of Classical Cepheids as standard candles is of paramount importance for astronomy. The recent advances in infrared space astronomy have shifted the focus of obtaining accurate PL relations to wavelengths longer than the visible, where interstellar extinction is reduced. Madore et al. (2009b) and Freedman et al. (2009) have demonstrated how PL relations obtained at IRAC wavelengths can be effectively used to measure the distance of nearby galaxies. This work is a further step in the characterization of PL relations in all *Spitzer* photometric bands, including two MIPS bands at 24 and 70 μm , by using a

sample of Classical Cepheids in the Galaxy.

In order to provide a detailed comparison between theory and observations we adopted the large set of nonlinear, convective models computed by Bono et al. (1999); Marconi et al. (2005) and by Fiorentino et al. (2007). For Galactic Cepheids we chose a scaled-solar chemical composition (helium, $Y = 0.28$; metals, $Z = 0.02$) and accounted for fundamental mode pulsators. Moreover, we covered a broad range of stellar masses ($3.5 \leq M/M_{\odot} \leq 11.5$), and to account for current uncertainties affecting the size of the helium core (Bono et al. 2006) we adopted two different mass-luminosity relations based on canonical and non-canonical (the latter incorporating a range of main sequence core convective overshoot) evolutionary models. Theoretical predictions were transformed into the observational plane using scaled-solar atmospheres based on ATLAS9 models (Castelli & Kurucz 2003), and multiplied with the IRAC band-passes. The slopes and zero points of these model Leavitt laws are listed in the last two columns of Table 6. While the zero points are in general agreement with all our fits, the slopes are significantly shallower than our best fits obtained with both “new” and “old” distances (the disagreement is however reduced in the fits adopting the “new” distances). The PL relations derived with the exclusive use of the astrometric distances (that do not rely on the $p(P)$ relation), are however in excellent agreement with the theoretical relations. This result may suggest that the period dependence of the p -factor currently adopted in IRSB distances may still need further refinement. Because of the small number of Cepheids and the limited range of periods for which accurate parallaxes are available, we could not attempt to invert the problem and estimate the $p(P)$ dependence with our data.

Comparison between our Galactic PL relations and the relations derived for the LMC by Madore et al. (2009a) and Ngeow et al. (2009) leads to contradictory results. The PL relations obtained with both the “new” and “old” IRSB distances are steeper than the LMC relations, while the Galactic PL relations we obtain with the astrometric distances are significantly shallower. To add to the confusion, it should be noted that the slopes derived by Ngeow et al. (2009) and Madore et al. (2009a) disagree by more than their respective uncertainties, despite using stars from the same galaxy³. The contradictory results in our Galactic PL relation slopes shows once more the effects of the systematics introduced by the IRSB distances and their dependence on the $p(P)$ relation. Based on the more reliable astrometric distances we should conclude that the slope of the PL relation could be shallower at Galactic metallicity than in the LMC, but even this result is not statistically significant, due to the larger uncertainty in the PL slope. In conclusion, the insufficient reliability of the

³The difference between the two LMC results can be an issue of crowding and binarity in the Ngeow et al. (2009) sample (selected without individual image inspection, and containing a larger fraction of fainter short period Cepheids) that could result in shallower slopes.

IRSB distances, and the small number of stars for which astrometric distances are available, prevents us from resolving the dependence of the PL relations from metallicity. This problem has already been noticed at optical and near-IR wavelengths by other authors (see e.g. Storm et al. 2004; Fouqué et al. 2007; Romaniello et al. 2008). Riess et al. (2009) also noted that the precision of current datasets does not allow measurement of the dependence of the PL relation on metallicity; those authors measured statistically consistent slopes at 1.6 micron for the Milky Way, the LMC and other galaxies.

We also cannot determine a reliable wavelength dependence of the PL slope, as all our values are within 1σ from the average slope value. This is consistent with the expected flattening of the PL slope wavelength dependence in the mid-IR shown by the models. If we compare our slope values with Figure 4 in Freedman et al. (2008), however, we note a similar trend. Our result for $4.5\ \mu\text{m}$ is marginally higher (by ~ 0.1) than the slope at the 3.6 and $8.0\ \mu\text{m}$, as also shown by the LMC Cepheid fit (and by the models). This anomaly in the $4.5\ \mu\text{m}$ (and, to a minor extent, $5.8\ \mu\text{m}$) slope is related to the presence of the variable CO band, which increases the amplitude variation in these bandpasses.

For the first time we have measured the PL relation in the MIPS 24 and $70\ \mu\text{m}$ bands. The $24\ \mu\text{m}$ relation, in particular, is important for the determination of Cepheid distances in the Galactic plane from datasets such as MIPS GAL (Carey et al. 2009), where high extinction from ISM dust may complicate their detection at IRAC bands.

The determination of a PC relation is in principle not limited by the uncertainty in the distances affecting our PL relations. Figure 5, however, clearly shows that such a relation can be derived with sufficient accuracy only in the $[3.6] - [8.0]$ color. Other colors show a scatter that is increasingly larger with the period, as high as ~ 0.1 mag, one order of magnitude larger than our color accuracy of ~ 0.02 . The fact that this scatter was not found by Ngeow et al. (2009) may again be a consequence of the difference in the median period between our Galactic and their LMC sample.

Based on our data and on numerical modeling of one representative Cepheid (ζ Gem), we conclude that the color scatter affecting long period Cepheids is a consequence of variable stellar CO absorption, rather than infrared excess from circumstellar dust. Circumstellar dust at ~ 500 K (the temperature where dust thermal emission is maximum in the IRAC bands) would produce the largest excess in the $[3.6] - [8.0]$ color, which we do not observe, with the possible exception of a weak detection (~ 0.1 mag) around Polaris. Our ζ Gem models show that scatter in the IRAC 4.5 and $5.8\ \mu\text{m}$ bands can be induced by variations in effective temperature and/or the propagation of shocks through the Cepheid atmospheres. A more comprehensive modeling effort, including Cepheids with different periods and pulsation modes, is however required to confirm and quantify this effect.

Not finding an infrared excess in most, if not all, stars is somewhat unexpected, given the detection of circumstellar shells by near-IR interferometers. Figure 8 in Mérand et al. (2007) shows a number of targets, including the long period Cepheids Y Oph and ℓ Car (both part of our sample), with a significant (4–5%) excess in the K band. We do not measure any excess of this magnitude in these or other stars, which seems to rule out the presence of circumstellar dust in the shells detected around these and other Cepheids. The interferometric determination of the radius of these circumstellar shells, however, indicate values as low as ~ 2 stellar radii (Mérand et al. 2006). For a Cepheid with $T_{\text{eff}} \sim 5,000\text{--}6,000$ K, dust equilibrium temperature at $\sim 2 R_*$ would be $T_d \simeq T_*/\sqrt{R_d/R_*} \lesssim 3,500$ K. This is well above the sublimation temperature of any known astronomical dust.

Our results can be reconciled with the interferometric detection of circumstellar shells close to the star if the emission is not due to dust, but rather to some strong molecular line emission. Given that the observations in Mérand et al. (2006, 2007) and Kervella et al. (2006) were made in the K band, a possible candidate for this emission is shocked H_2 . The presence of H_2 shocked emission lines could further contribute to the scatter in the IRAC 4.5 μm band, for certain densities and shock velocities (Smith et al. 2006). This hypothesis supports the idea that Cepheid stars indeed have a strong stellar wind associated with a pulsation driven mass-loss mechanism, as suggested by Mérand et al. (2007). Unlike the case of mass loss in red giants, AGB and supergiant stars (showing a dust-driven wind), this stellar wind would be largely dustless, due to the higher temperature of the star. This hypothesis needs to be tested by near-IR multi-epoch spectral monitoring of these stars.

This hypothesis does not imply that a Cepheid stellar wind is completely devoid of dust, that may be condensing at larger radii, in quantities below the detection limits of our IRAC observations (see ℓ Car mid-IR detection of mid-IR circumstellar emission with the VLT MIDI and VISIR instruments, Kervella et al. 2009). Cold dust may also be collected by the outflow, at much larger distances (thousands of AU), from the ISM, as in the case of the well known nebula around RS Pup (Kervella et al. 2009). We find evidence supporting this mechanism in our IRAC and MIPS images. Extended emission at 5.8, 8.0, 24 and 70 μm around δ Cep indicate that this star may be losing mass due to a strong wind pushing into the local interstellar medium, which is leading to the formation of a 70 μm bow shock detected at large distance from the star ($\sim 10,000$ AU). A detailed analysis of this phenomenon is being published elsewhere (Marengo et al., in preparation). In a more comprehensive paper (Barmby et al. 2009) we will discuss the presence of spatially resolved extended emission at 24 and 70 μm around more targets, and quantify the occurrence of mass loss in the Cepheid phase that can be inferred from our imaging data.

8. Summary

We have derived the PL and PC relations in *Spitzer*/IRAC bands for a sample of Galactic Cepheids. These relations are critically dependent on the choice of the period dependence of the p -factors used for the distance determination with the IRSB method, even though the uncertainties in our fits prevent the assessment of the best $p(P)$ relation choice. The best agreement with theoretical PL relations, however, is obtained when only distances obtained by astrometric methods are used. We do not detect statistically significant variations between the slope and zero points of the PL relations between our Galactic sample and LMC relations obtained by Madore et al. (2009a), despite the difference in metallicity. We find that the intrinsic variations in the 4.5 and 5.8 μm fluxes are larger for long period Cepheids. These variations (of the order of ~ 0.1 mag) are related to deep CO absorption, dependent on the stellar T_{eff} and hydrodynamic effects associated to the stellar pulsations. We do not find significant infrared excess related to warm circumstellar dust, except for a weak excess detected at IRAC wavelengths for Polaris, and at 70 μm for SZ Tau. This may rule out the presence of extensive dust driven mass loss in the Cepheid phase, but leaves open the possibility of pulsation-driven mass loss from a dust-poor wind, as suggested by recent interferometric observations.

This work is based on observations made with the *Spitzer* Space Telescope, which is operated by the Jet Propulsion Laboratory, California Institute of Technology under NASA contract 1407. P. B. and D. W. both acknowledge research support through Discovery Grants from the Natural Sciences and Engineering Research Council of Canada. N. R. E. acknowledges support from the Chandra X-Ray Center grant NAS8-03060. We thank Robert Kurucz and Chow-Choong Ngeow for helpful discussions during the preparation of this manuscript. We also acknowledge M. Marconi and P.G. Prada Moroni for sending us the predicted Cepheid PL relations in advance of publication.

Facilities: Spitzer (IRAC, MIPS).

REFERENCES

- Alcock, C. et al. 2005, AJ, 109, 1653
Barmby, P. et al. 2009, in preparation
Barnes, T. G., Storm, J., Jefferys, W. H., Gieren, W. P. & Fouqué, P. 2005, ApJ, 631, 572
Beaulieu, J. P., Buchler, J. R. & Kollath, Z. 2001, A&A, 373, 164

- Beichman, C. A., Neugebauer, G., Habing, H. J., Clegg, P. E. & Chester, T. J. (editors) 1985, *Infrared Astronomy Satellite (IRAS) Catalog and Atlases Explanatory Supplement* (Jet Propulsion Laboratory, Pasadena)
- Benedict, G. F. et al. 2007, *AJ*, 133, 1810
- Bono, G., Marconi, M. & Stellingferf, R. F. 1999, *ApJS*, 122, 167
- Bono, G., Caputo, F., Cassisi, S., Marconi, M., Piersanti, L. & Tornambé, A. 2000, *ApJ*, 543, 955
- Bono, G., Gieren, W. Marconi, M., Fouqué & P. Caputo, F. 2001, *ApJ*, 563, 319
- Bono, G., Castellani, V. & Marconi, M. 2002, *ApJ*, 565, L83
- Bono, G. et al. 2006, *Mem. SAI*, 77, 207
- Caputo, F., Bono, G., Fiorentino, G., Marconi, M. & Musella, I. 2005, *ApJ*, 629, 1021
- Carey, S. J. et al. 2009, *PASP*, 121, 875
- Carpenter, J. M., Bouwman, J., Silverstone, M. D., Kim, J. S., Stauffer, J., Cohen, M., Hines, D. C., Meyer, M. R., & Crockett, N. 2008, *ApJS*, 179, 423
- Castellani, V. et al. 2005, *ApJ*, 539, 928
- Castelli, F. & Kurucz, R. 2003, in *IAU Symp. 210, Modelling of Stellar Atmospheres*, ed. N.E. Piskunov, W.W. Weiss, D.F. Gray, (San Francisco: ASP), 20
- Deasy, H. P. 1988, *MNRAS*, 231, 673
- de Jager C. & Nieuwenhuijzen, H. 1997, *MNRAS*, 290, L50
- Engelbracht, C. W. et al. 2007, *PASP*, 119, 994
- Evans, N.R., Böhm-Vitense, E., Karpenter, K., Beck-Winchatz, B. & Robinson, R. 1997, *PASP*, 109, 789
- Evans, N.R., Massa, D. Fullerton, A., Sonnerbon, G. & Iping, R. 2006, *ApJ*, 647, 1387
- Evans, N. R., Schaefer, G. H., Bond, H. E., Bono, G., Karovska, M., Nelan, E., Sasselov, D. & Mason, B. 2008, *AJ*, 136, 1137
- Evans, N. R., Massa, D. & Proffitt, C. 2009, *AJ*, 137, 3700

- Fazio, G. G. et al. 2004, ApJS, 154, 10
- Feast, M. W. & Catchpole, R. M. 1997, MNRAS, 286, L1
- Fernie, J. D., Beattie, B., Evans, N. R. & Seager, S. 1995, Int. Bulletin of Variable Stars No. 4148
- Fiorentino, G., Marconi, M., Musella, I. & Caputo, F. 2007, A&A 476, 863
- Flaherty, K. M., Pipher, J. L., Megeath, S. T., Winston, E. M., Gutermuth, R. A., Muzerolle, J., Allen, L. & Fazio, G. G. 2007, ApJ, 663, 1069
- Fouqué, P. & Gieren, W. P. 1997, A&A, 320, 799
- Fouque, P. et al. 2007, A&A, 476, 73
- Freedman, W. L., Madore, B. F., Rigby, J. & Persson, S. E. 2008, ApJ, 679, 71
- Freedman, W. L., Rigby, J., Madore, B. F., Persson, S. E., Sturch, L. & Mager, V., ApJ, 695, 996
- Fricke, K., Stobie, R. S. & Strittmatter, P. A. 1972, ApJ, 171, 593
- Gieren, W. P., Barnes, T. G. & Moffett, T. J. 1993, ApJ, 418, 135
- Gordon, K. D. et al. 2007, PASP, 119, 1019
- Groenewegen, M. A. T., Romaniello, M., Primas, F. & Mottini, M. 2004, A&A, 420, 655
- Hora, J. L. et al. 2008, PASP, 120, 1233
- Indebetouw, R. et al. 2005, ApJ, 619, 931
- Keller, S. C. & Wood, P. R. 2006, ApJ, 642, 834
- Kervella, P., Nardetto, N., Bersier, D., Mourard, D. & Coudé du Foresto, V. 2004, A&A, 416, 941
- Kervella, P., Mérand, A., Perrin, G. & Coudé Du Foresto, V. 2006, A&A, 448, 623
- Kervella, P., Mérand, A., Szabados, L., Fouqué, P., Bersier, D., Pompei, E. & Perrin, G. 2008, A&A, 480, 167
- Kervella, P., Mérand, A. & Gallenne, A. 2009, A&A, 498, 425
- Lane, B. F., Creech-Eakman, M. J. & Nordgren, T. E. 2002, ApJ, 573, 330

- Leavitt, H.S. 1908, *Ann. Harvard Obs.* 15, 4, 87
- Lutz, D. et al. 1996, *A&A*, 315, L269
- Madore, B. F., Freedman, W. L., Rigby, J., Persson, S. E., Sturch, L. & Mager, V. 2009a, *ApJ*, 695, 988
- Madore, B. F., Rigby, J., Freedman, W. L., Persson, S. E., Sturch, L. & Mager, V. 2009b, *ApJ*, 639, 936
- Marconi, M., Musella, I. & Fiorentino, G. 2005, *AJ*, 632, 590
- Marengo, M., Sasselov, D. D., Karovska, M., Papaliolios, C. & Armstrong, J. T. 2002, *ApJ*, 567, 1131
- Marengo, M., Karovska, M., Sasselov, D. D., Papaliolios, D., Armstrong, J. T. & Nordgren, T. E. 2003, *ApJ*, 589, 968
- Marengo, M., Karovska, M., Sasselov, D. D. & Sanchez, M. C. 2004, *ApJ*, 603, 285
- Marengo, M., Reiter, M. & Fazio, G. G. 2008, in proc. “IX Torino Workshop on Evolution and Nucleosynthesis in AGB Stars and the IIIInd Perugia Workshop on Nuclear Astrophysics”, *AIP Conf. Series* vol. 1001, p. 331
- Marengo, M., Stapelfeldt, K., Werner, M. W., Hora, J. L., Fazio, G. G., Schuster, M. T., Carson, J. C. & Megeath, S. T. 2009a, *ApJ*, 700, 1647
- Marengo, M., Evans, N. R., Barmby, P., Bono, G. & Welch, D. 2009b, in proc. “The Evolving ISM in the Milky Way and Nearby Galaxies”, eds. K. Sheth, A. Noriega-Crespo, published online at <http://ssc.spitzer.caltech.edu/mtgs/ismevol>
- McAlary, C. W. & Welch, D. L. 1986, *AJ*, 91, 1209
- Meixner, M., et al. 2006, *AJ*, 132, 2268
- Mérand, A. et al. 2006, *A&A*, 453, 155
- Mérand, A. et al. 2007, *A&A*, 664, 1093
- Moskalik, P. Buchler, J.R. & Marom, A. 1992, *ApJ*, 385, 685
- Moskalik, P. & Gorynya, N. A. 2005, *Acta Astronomica*, 55, 247
- Nardetto, N., Mourard, D., Mathias, P., Fokin, A. & Gillet, D. 2007, *A&A*, 471, 661

- Ngeow, C. & Kanbur, S. M. 2008, *ApJ*, 679, 76
- Ngeow, C.-C., Kanbur, S. M., Neilson, H. R., Nanthakumar, A., & Buonaccorsi, J. 2009, *ApJ*, 693, 691
- Neilson, H. R., Ngeow, C.-C., Kanbur, S. M., & Lester, J. B. 2009, *ApJ*, 692, 81
- Nordgren, T. E., Armstrong, J. T., Germain, M. E., Hindsley, R. B., Hajian, A. R., Sudol, J. J. & Hummel, C.A. 2000, *ApJ*, 543, 972
- Pedicelli, S. et al. 2009, *A&A*, 504, 81
- Reimers, D., 1975, *Mem. Soc. Roy. Sci. Liege 6th Ser.*, 8, 369
- Rieke, G. H. & Lebofsky, M. J. 1985, *ApJ*, 288, 618
- Rieke, G. et al. 2004, *ApJS*, 154, 25
- Riess, A. et al. 2005, *ApJ*, 627, 579
- Riess, A. G. et al. 2009, *ApJ*, 699, 539
- Rogers, F. J. & Iglesias, C. A. 1992, *ApJ*, 401, 316
- Romaniello, M. et al. 2008, *ApJ*, 488, 731
- Román-Zúñiga, C. G., Lada, C. J., Muench, A. & Alves, J. F. 2007, *ApJ*, 664, 357
- Sandage, A., Tammann, G. A. & Reindl, B. 2004, *A&A*, 424, 43
- Sandage, A., Tammann, G. A. & Reindl, B. 2009, *A&A*, 493, 471
- Schuster, M. T., Marengo, M. & Patten, B. M. 2006 SPIE meeting, Orlando FL, #6720-65
- Seaton, M.J., Yan, Y. Mihalas, D. & Pradhan, A. K. 1994, *MNRAS*, 266, 805
- Serenelli, A. & Weiss, A. 2005, *A&A*, 442, 1041
- Smith, H. A., Hora, J. L., Marengo, M. & Pipher, J. L. 2006, *ApJ*, 645, 1264
- Spitoni, E., Matteucci, F., Recchi, S., Cescutti, G. & Pipino, A. 2009, *A&A*, 504, 87
- Storm, J., Carney, B. W., Gieren, W. P., Fouqué, P., Latham, D. W. & Fry, A. M. 2004, *A&A*, 415, 531
- Tammann, G. A., Sandage, A. & Reindl, B. 2003, *A&A*, 404, 423

Udalski, A., Szymanski, M., Kubiak, M., Pietrzynski, G., Soszynski, I., Wozniak, P. & Zebrun, K. 1999, *Acta Astron.*, 49, 223

van Leeuwen, F., Feast, M. W., Whitelock, P. A. & Laney, C.D. 2007, *MNRAS*, 379, 723

Welch, D. L., Wieland, F., McAlary, C. E., McGonegal, R., Madore, B. F., McLaren, R. A. & Neugebauer, G. 1984, *ApJS*, 54, 574

Werner, M. W. et al. 2004, *ApJS*, 154, 1

Willson, L. A. 2000, *ARA&A*, 38, 573

Yong et al. 2000, *ApJ*, 539, 928

Table 1. Target list and catalog of observations

Name	IRAC sub JD ^a	IRAC full JD ^a	MIPS JD ^a	D [kpc] ^b	D [kpc] ^c	P [d]	Mode
DT Cyg	54065.535	...	53935.208	0.457 ± 0.069	0.535 ± 0.029^d	2.54	1st
SZ Tau	54006.076	54189.135	54400.742	0.513 ± 0.029	0.556 ± 0.034^e	3.15	1st
RT Aur	54036.201	...	54202.804	0.417 ± 0.033^f	0.417 ± 0.033^f	3.73	F
Polaris ⁱ	...	52991.065	54024.680	0.130 ± 0.002^f	0.130 ± 0.002^f	3.97	1st
BF Oph	53997.204	...	53979.664	0.637 ± 0.032	0.714 ± 0.011	4.07	F
FF Aql ⁱ	54039.420	...	54023.113	0.356 ± 0.023^f	0.356 ± 0.023^f	4.47	F
V350 Sgr ⁱ	54002.135	...	54013.655	0.935 ± 0.052	0.979 ± 0.054^d	5.15	F
δ Cep	...	53957.101	53935.018	0.273 ± 0.011^f	0.273 ± 0.011^f	5.37	F
V Cen	53957.367	53957.365	53980.875	0.606 ± 0.044	0.684 ± 0.020	5.49	F
BB Sgr	54002.629	...	54013.643	0.787 ± 0.031	0.801 ± 0.010	6.64	F
U Sgr	53999.677	53997.790	54009.048	0.565 ± 0.019	0.585 ± 0.006	6.75	F
V636 Sco ⁱ	53997.194	...	53983.521	...	0.839 ± 0.046^d	6.80	F
U Aql ⁱ	54039.442	...	54016.545	0.606 ± 0.029	0.691 ± 0.038^d	7.02	F
η Aql	...	54039.439	54238.612	0.241 ± 0.014	0.250 ± 0.005	7.18	F
W Sgr ⁱ	53997.264	...	54013.542	0.439 ± 0.038^f	0.439 ± 0.038^f	7.59	F
GH Lup	53961.333	...	53979.733	1.124 ± 0.203	1.023 ± 0.051^g	9.28	F
S Mus ⁱ	53960.571	...	53935.332	0.820 ± 0.054	0.916 ± 0.046^g	9.66	F
S Nor	53999.638	54351.249	53983.802	0.943 ± 0.044	0.959 ± 0.014	9.75	F
β Dor	...	53960.988	53935.322	0.318 ± 0.016^f	0.318 ± 0.016^f	9.84	F
ζ Gem	...	54228.830	54046.15	0.360 ± 0.023^f	0.360 ± 0.023^f	10.15	F
X Cyg	54065.539	...	53935.023	1.163 ± 0.027	1.213 ± 0.010	16.39	F
Y Oph	53997.328	...	54202.088	0.552 ± 0.040	0.573 ± 0.008^h	17.13	F
VY Car	53957.067	...	53935.360	1.818 ± 0.099	1.994 ± 0.020	18.91	F
SW Vel	54098.538	...	54202.474	2.381 ± 0.057	2.506 ± 0.029	23.44	F
T Mon ⁱ	54395.313	...	54021.550	1.389 ± 0.058	1.455 ± 0.037	27.02	F
AQ Pup	54228.851	...	54107.409	3.030 ± 0.184	3.194 ± 0.066	30.10	F
ℓ Car	...	53960.984	53935.328	0.498 ± 0.050^f	0.498 ± 0.050^f	35.55	F
U Car	53960.567	...	53935.349	1.492 ± 0.067	1.565 ± 0.023	38.77	F

Table 1—Continued

Name	IRAC sub JD ^a	IRAC full JD ^a	MIPS JD ^a	D [kpc] ^b	D [kpc] ^c	P [d]	Mode
RS Pup	54098.477	...	54073.425	1.818±0.099	2.052±0.151	41.39	F
HD183864 ^j	54064.419	...	54046.098
HD182296 ^j	54226.294	...	54018.537
γ Phe ^j	53957.014	...	53935.315
ψ And ^j	...	54094.302	54106.889

^aJD-2400000.5 at observation start

^bDistance from Fouqué et al. (2007) unless noted

^cDistance from Storm et al. (2004) unless noted

^dThis work (Table 2)

^eDistance from Groenewegen et al. (2004)

^fDistance from Benedict et al. (2007) or van Leeuwen et al. (2007) for Polaris

^gDistance from Romaniello et al. (2008) (with 5% assumed uncertainty)

^hDistance from Barnes et al. (2005), Least Square fit

ⁱSpectroscopic binary

^jSupergiant or M giant (γ Phe) star

Table 2. “Old” distances missing from previous catalogs

Name	$R_0[R_\odot]$	θ_0 [mas]	V	K	$E(B - V)$	V_0	K_0	d [kpc]
DT Cyg	30.7 ± 0.9	0.570 ± 0.018	5.744 ± 0.010	4.430 ± 0.010	0.039 ± 0.020	5.635 ± 0.010	4.416 ± 0.010	0.535 ± 0.029
V350 Sgr	40.7 ± 4.5	0.424 ± 0.047	7.483 ± 0.010	5.141 ± 0.010	0.312 ± 0.020	6.516 ± 0.010	5.031 ± 0.010	0.979 ± 0.054
V636 Sco	50.0 ± 4.8	0.568 ± 0.054	6.654 ± 0.010	4.409 ± 0.010	0.217 ± 0.020	5.981 ± 0.010	4.332 ± 0.010	0.839 ± 0.046
U Aql	51.3 ± 6.0	0.830 ± 0.097	6.446 ± 0.010	3.893 ± 0.010	0.399 ± 0.020	5.209 ± 0.010	3.752 ± 0.010	0.691 ± 0.038

Table 3. IRAC and MIPS photometric calibration

Item	[3.6]	[4.5]	[5.8]	[8.0]	[24]	[70]
Isophotal λ [μm]	3.550	4.493	5.731	7.872	23.68	71.42
FLUXCONV [(MJy/sr)/(DN/s)]	0.1088	0.1388	0.5952	0.2021	0.0447	702.
6.1" aperture corr. [mag] ^a	0.051 \pm 0.002	0.055 \pm 0.002	0.056 \pm 0.006	0.065 \pm 0.005
f_{corr} (subarray)	0.994	0.995	0.939	1.006
F_{ν} (Vega) [Jy]	280.9 \pm 4.1	179.7 \pm 2.6	115.0 \pm 1.7	64.1 \pm 0.9	7.14 \pm 0.08	0.775 \pm 0.009

^aAperture used for FF Aql, VY Car and AQ Pup IRAC subarray data

Table 4. IRAC aperture vs. PSF fitting photometry comparison^a

Name	IRAC mode	[3.6]	[4.5]	[5.8]	[8.0]
V Cen	subarray	4.336±0.010	4.356±0.010	4.377±0.003	4.347±0.003
"	full frame	4.332±0.270	4.392±0.156	4.392±0.093	4.362±0.060
U Sgr	subarray	3.811±0.010	3.856±0.010	3.864±0.008	3.829±0.006
"	full frame	3.844±0.236	3.772±0.105	3.789±0.054	3.789±0.053
S Nor	subarray	3.969±0.010	4.015±0.010	4.035±0.008	4.000±0.006
"	full frame	3.984±0.150	4.072±0.136	4.027±0.067	4.005±0.044
SZ Tau	subarray	4.165±0.010	4.164±0.010	4.206±0.009	4.185±0.007
"	full frame	4.144±0.200	4.144±0.200	4.221±0.080	4.195±0.076
Avg diff.	...	-0.007±0.021	0.009±0.065	0.021±0.049	0.003±0.022

^aWith the exception of V Cen, full frame and subarray data of each source have been obtained at different epochs, and the difference in photometry can be related not only on photometry biases, but also to the source variability

Table 5. Final *Spitzer* photometry of all targets

Name	IRAC mode	[3.6]	[4.5]	[5.8]	[8.0]	[24]	[70]
DT Cyg	subarray	4.340±0.010	4.342±0.011	4.381±0.010	4.386±0.008	4.367±0.002	3.791±0.257
SZ Tau	subarray	4.165±0.010	4.164±0.010	4.206±0.009	4.185±0.007	4.209±0.002	3.013±0.195
RT Aur	subarray	3.865±0.010	3.880±0.010	3.924±0.008	3.914±0.006	3.773±0.002	3.645
Polaris	full frame	0.573±0.037	0.493±0.051	0.411±0.070	0.459±0.042	0.723±0.001	0.506±0.050
BF Oph	subarray	5.141±0.010	5.136±0.010	5.171±0.005	5.162±0.004	5.031±0.005	3.698
FF Aql	subarray	3.391±0.010	3.390±0.010	3.436±0.008	3.428±0.007	3.338±0.001	3.458
V350 Sgr	subarray	4.948±0.010	4.957±0.010	4.988±0.004	4.988±0.003	5.032±0.009	3.991
δ Cep	full frame	2.174±0.044	2.182±0.037	2.166±0.032	2.150±0.039	2.120±0.001	2.174
V Cen	subarray	4.336±0.010	4.356±0.010	4.377±0.003	4.347±0.003	4.424±0.003	2.813
BB Sgr	subarray	4.350±0.010	4.380±0.010	4.386±0.003	4.370±0.003	4.339±0.004	3.814
U Sgr	subarray	3.811±0.010	3.856±0.010	3.864±0.008	3.829±0.006	3.760±0.003	1.910
V636 Sco	subarray	4.375±0.010	4.389±0.011	4.434±0.010	4.400±0.008	4.384±0.001	2.913
U Aql	subarray	3.810±0.010	3.869±0.010	3.877±0.008	3.839±0.006	3.665±0.002	3.682±0.294
η Aql	full frame	2.003±0.041	1.997±0.048	1.990±0.021	1.970±0.047	1.856±0.001	1.860±0.165
W Sgr	subarray	2.787±0.010	2.855±0.010	2.877±0.005	2.825±0.004	2.808±0.001	2.154
GH Lup	subarray	4.692±0.010	4.716±0.010	4.731±0.004	4.706±0.003	4.644±0.006	2.085
S Mus	subarray	3.835±0.010	3.845±0.010	3.884±0.008	3.877±0.006	3.902±0.001	3.156±0.278
S Nor	subarray	3.969±0.010	4.015±0.010	4.035±0.008	4.000±0.006	4.086±0.002	3.102
β Dor	full frame	1.899±0.059	1.990±0.068	1.937±0.049	1.880±0.037	1.858±0.001	1.864±0.103
ζ Gem	full frame	2.045±0.039	2.045±0.032	2.060±0.033	2.045±0.032	1.982±0.001	1.799±0.124
X Cyg	subarray	3.741±0.010	3.880±0.010	3.841±0.007	3.765±0.006	3.680±0.001	3.352
Y Oph	subarray	2.543±0.010	2.510±0.010	2.566±0.004	2.556±0.003	2.509±0.001	2.965
VY Car	subarray	4.497±0.010	4.591±0.010	4.580±0.007	4.505±0.006	4.527±0.006	2.391
SW Vel	subarray	4.891±0.010	4.908±0.010	4.919±0.006	4.887±0.003	5.064±0.003	4.302
T Mon	subarray	3.309±0.010	3.469±0.010	3.428±0.006	3.320±0.005	3.422±0.001	2.978
AQ Pup	subarray	5.014±0.010	4.982±0.010	5.009±0.007	4.993±0.006	4.889±0.004	4.171
ℓ Car	full frame	1.020±0.028	1.020±0.049	1.003±0.048	0.927±0.033	0.720±0.001	0.690±0.053

Table 5—Continued

Name	IRAC mode	[3.6]	[4.5]	[5.8]	[8.0]	[24]	[70]
U Car	subarray	3.543±0.010	3.694±0.010	3.654±0.007	3.535±0.005	3.187±0.006	0.454
RS Pup	subarray	3.324±0.010	3.336±0.010	3.350±0.006	3.331±0.005	3.316±0.001	-0.068
HD183864	subarray	4.281±0.010	4.311±0.011	4.321±0.010	4.310±0.007	4.247±0.002	3.959
HD182296	subarray	4.006±0.010	4.076±0.010	4.098±0.009	4.038±0.006	3.993±0.002	3.361
γ Phe	subarray	-0.627±0.048	-0.526±0.149	-0.504±0.121	-0.531±0.211
ψ And	full frame	2.415±0.076	2.507±0.084	2.462±0.037	2.389±0.034	2.332±0.001	2.307±0.157

Note. — Magnitudes without errors are lower limits (flux upper limits)

Table 6. PL relation coefficients for different samples

Band	“New” distances ^a		Astr. distances ^b		“Old” distances ^c		Model (Z=0.02, Y=0.28) ^d	
	α	β	α	β	α	β	α	β
3.6	-3.47 ± 0.06	-5.72 ± 0.07	-3.16 ± 0.22	-5.74 ± 0.18	-3.54 ± 0.04	-5.76 ± 0.04	-3.13 ± 0.01	-5.79 ± 0.01
4.5	-3.38 ± 0.06	-5.68 ± 0.07	-3.06 ± 0.23	-5.74 ± 0.19	-3.45 ± 0.04	-5.72 ± 0.04	-3.04 ± 0.01	-5.71 ± 0.01
5.8	-3.44 ± 0.06	-5.68 ± 0.07	-3.10 ± 0.23	-5.75 ± 0.19	-3.51 ± 0.03	-5.70 ± 0.04	-3.07 ± 0.01	-5.76 ± 0.01
8.0	-3.46 ± 0.06	-5.73 ± 0.07	-3.16 ± 0.22	-5.80 ± 0.18	-3.57 ± 0.03	-5.74 ± 0.04	-3.12 ± 0.01	-5.80 ± 0.01
24	-3.52 ± 0.06	-5.71 ± 0.06	-3.51 ± 0.21	-5.75 ± 0.17	-3.67 ± 0.03	-5.78 ± 0.03
70	-3.18 ± 0.26	-5.87 ± 0.22	-3.34 ± 0.27	-5.87 ± 0.23	-3.10 ± 0.25	-5.89 ± 0.22
<i>K</i>	-3.37 ± 0.06	-5.65 ± 0.02	-3.32 ± 0.12	-5.71 ± 0.03	-3.67 ± 0.12	-5.69 ± 0.03

^aDistances from Fouqué et al. (2007), Benedict et al. (2007) or van Leeuwen et al. (2007)

^bDistances from Benedict et al. (2007) or van Leeuwen et al. (2007)

^cDistances from Storm et al. (2004), Groenewegen et al. (2004), Barnes et al. (2005), Benedict et al. (2007), van Leeuwen et al. (2007) or this work (Table 2)

^dBased on the models described in Section 7

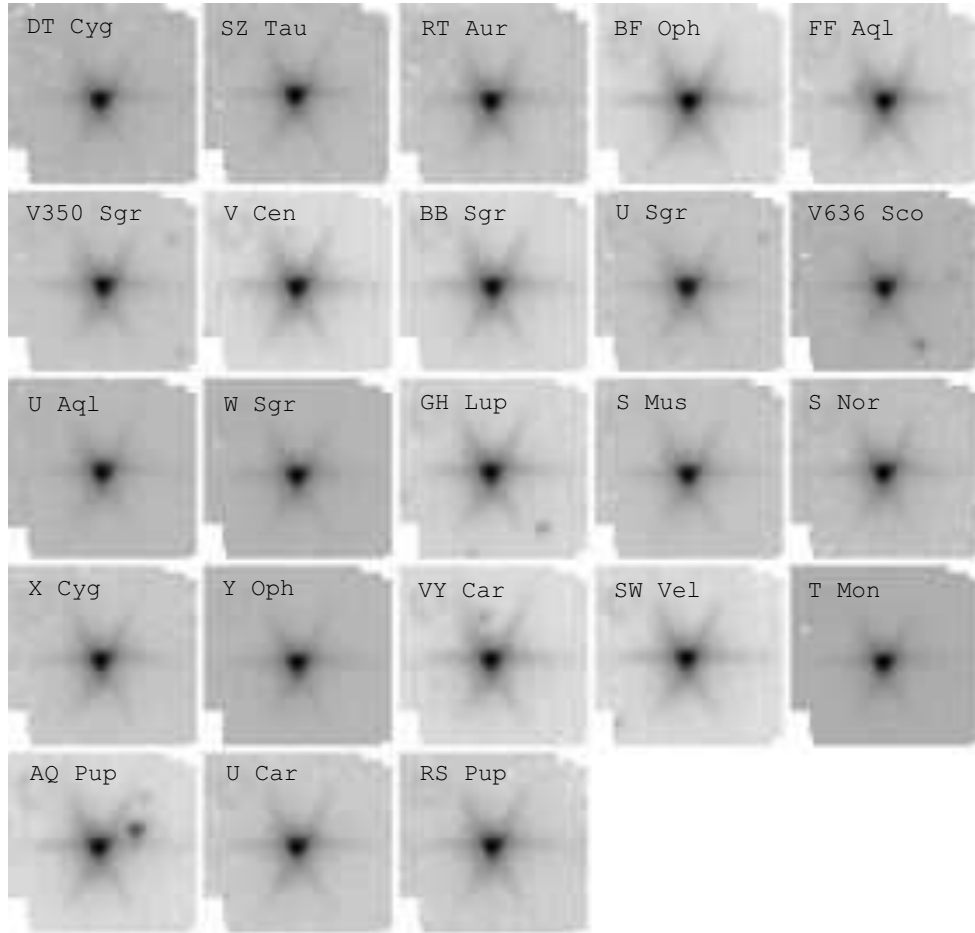


Fig. 1.— Thumbnail images of the 23 Cepheids observed in the IRAC subarray mode at $3.6 \mu\text{m}$, shown with a logarithmic color scale. The size of each thumbnail is about 45×45 arcsec. Only three targets (FF Aql, VY Car and AQ Pup) show one or more background stars within the standard 12.2 arcsec radius aperture used to measure the stars photometry. For these three stars a smaller 6.1 arcsec radius aperture has been used.

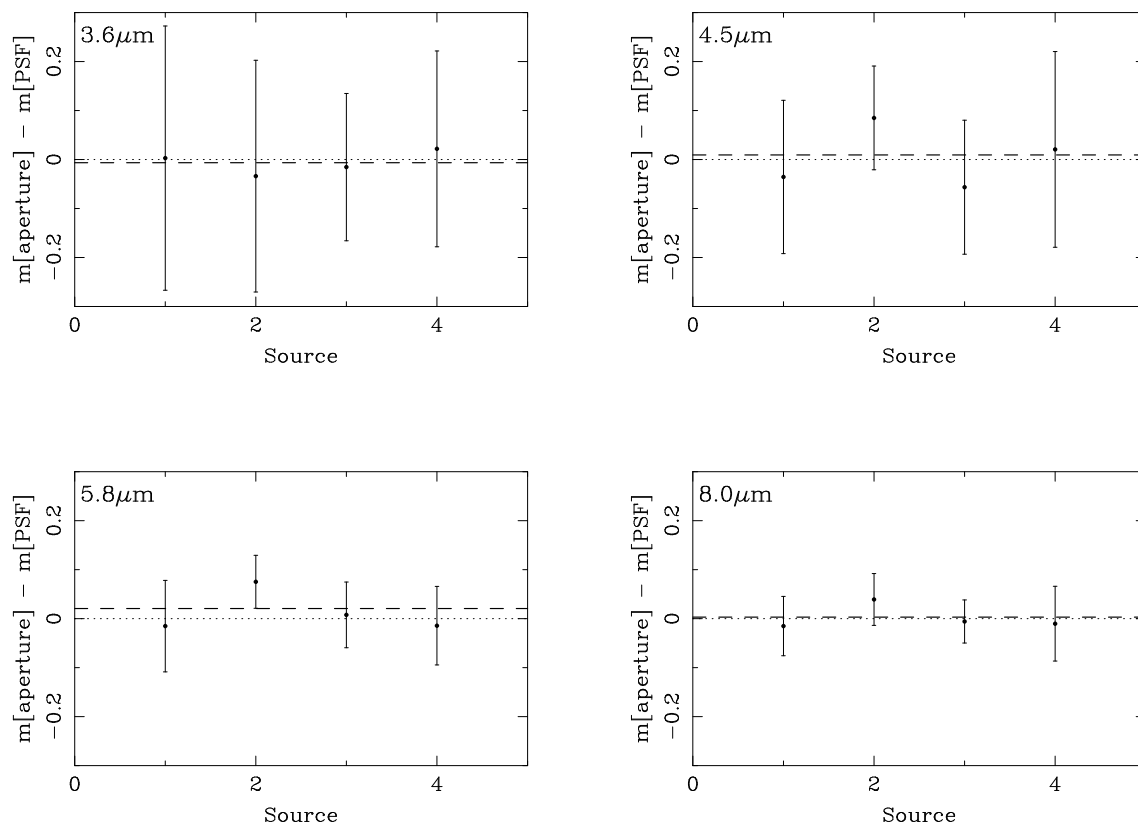


Fig. 2.— Comparison between aperture and PSF fitting photometry of four stars in our sample: #1 V Cen, #2 U Sgr, #3 S Nor and #4 SZ Tau. The error bars are the combined uncertainty of the offset between the aperture and PSF-fitting magnitudes. The dashed line is the average offset between the two sets of measurements (much smaller than the photometric error of each data-point). Note that only V Cen was observed in both subarray and full frame at the same epoch.

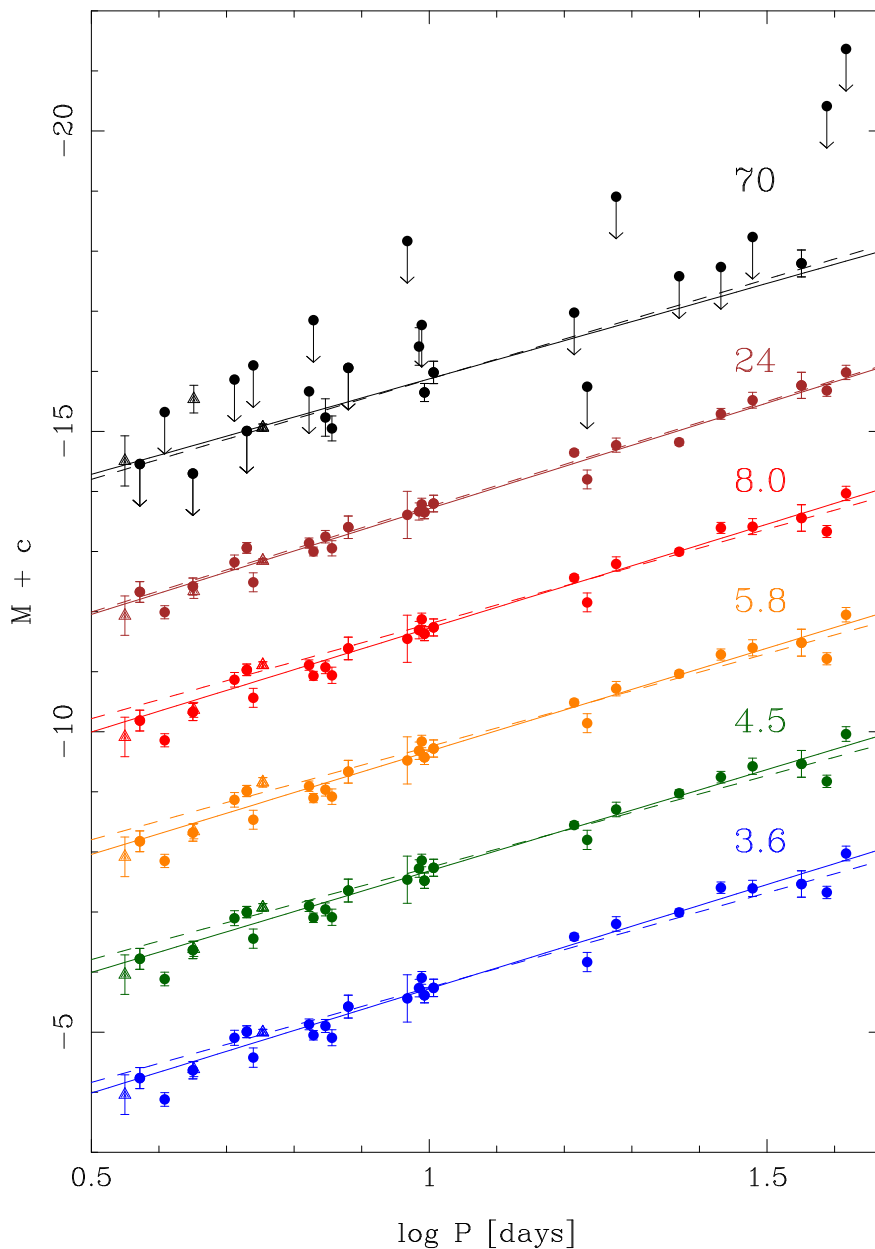


Fig. 3.— Period vs. absolute magnitude plots for all IRAC and MIPS bands. Circles are fundamental mode Cepheids while triangles are first overtone (with period “fundamentalized” using the relation from Feast & Catchpole 1997). This plot shows 3σ error bars for IRAC subarray photometry and the uncertainty listed in Table 1 for all other datapoints. The solid line shows the best-fit PL relation using all the distances from Fouqué et al. (2007), while the dashed line uses only stars with astrometric distances.

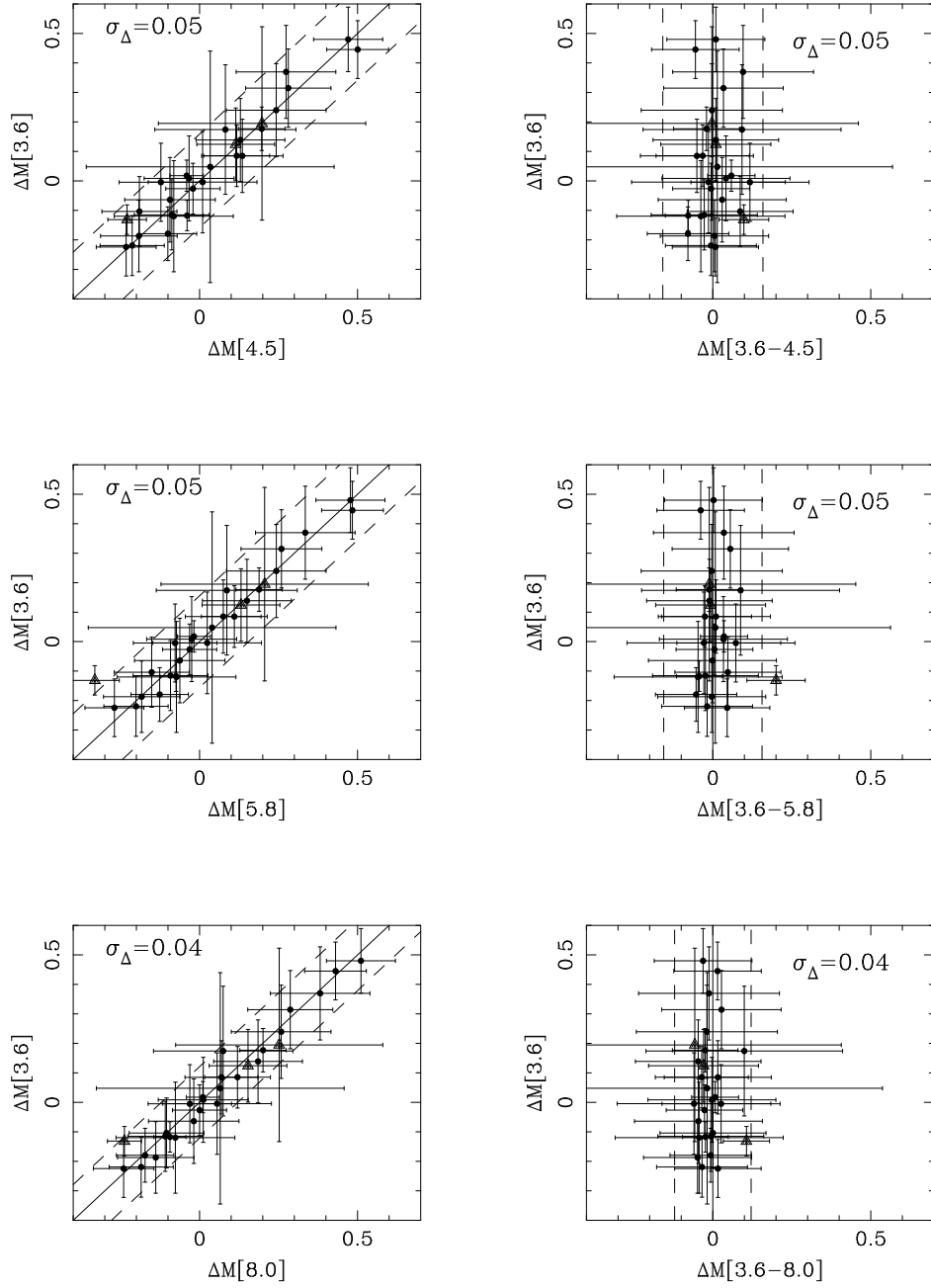


Fig. 4.— *Left panel* — Correlated residuals from the PL relation. *Right panel* — Color residuals from the PL relation. Circles are fundamental mode Cepheids, while triangles are first overtone. The two dashed lines show the $3\sigma_{\Delta}$ scatter around the unity-slope line (solid line).

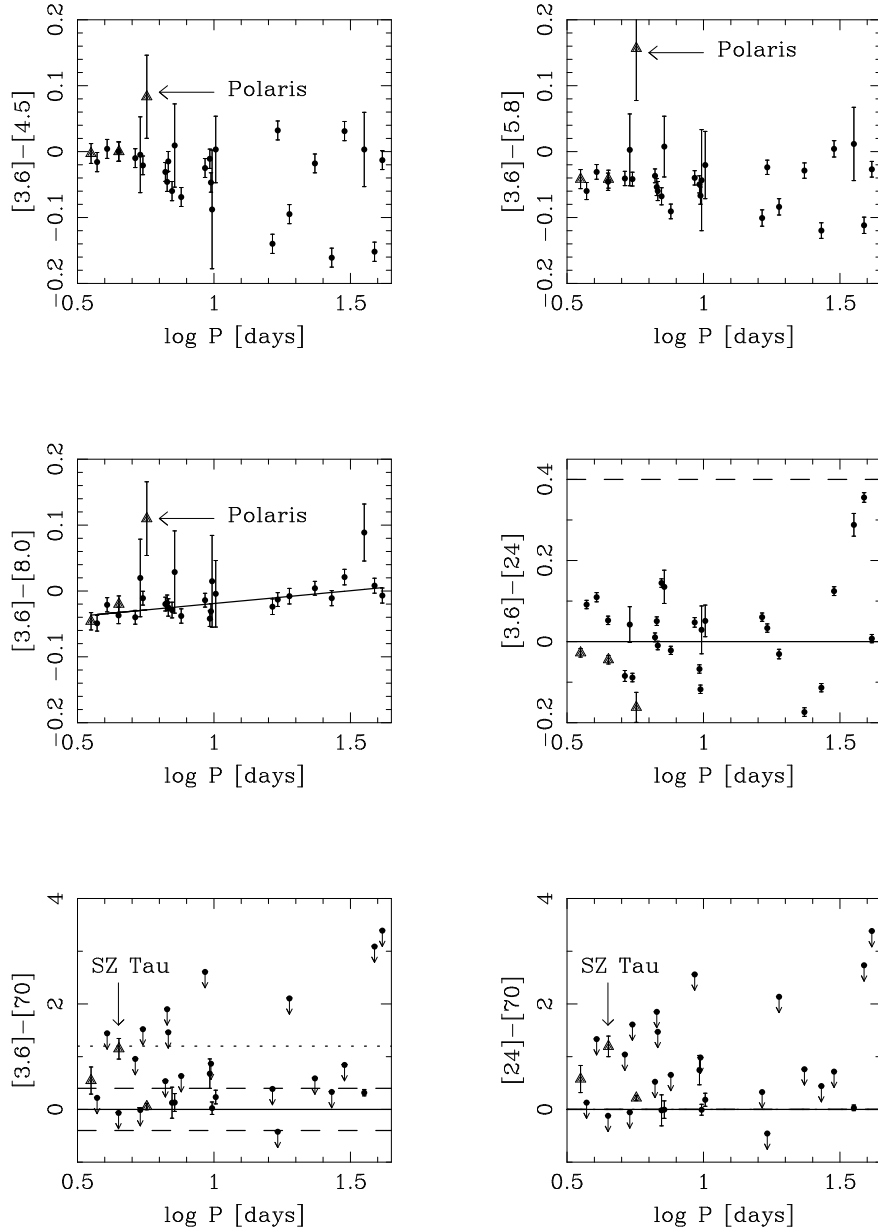


Fig. 5.— *Spitzer* colors vs. period for our sample. The solid line in the $[3.6] - [4.5]$ color panel is the best fit PC relation. The solid line in the other panels, when present, is a marker for the zero color of Rayleigh-Jeans atmospheres). The dashed and dotted lines indicate the 1 and 3σ dispersion expected for the $3.6\ \mu\text{m}$ lightcurve amplitude estimated in Section 5.1. Circles are fundamental mode Cepheids and triangles first overtone. SZ Tau has a $[24] - [70]$ color excess above 3σ the noise level, and Polaris has consistently red (~ 0.1 mag) IRAC colors.

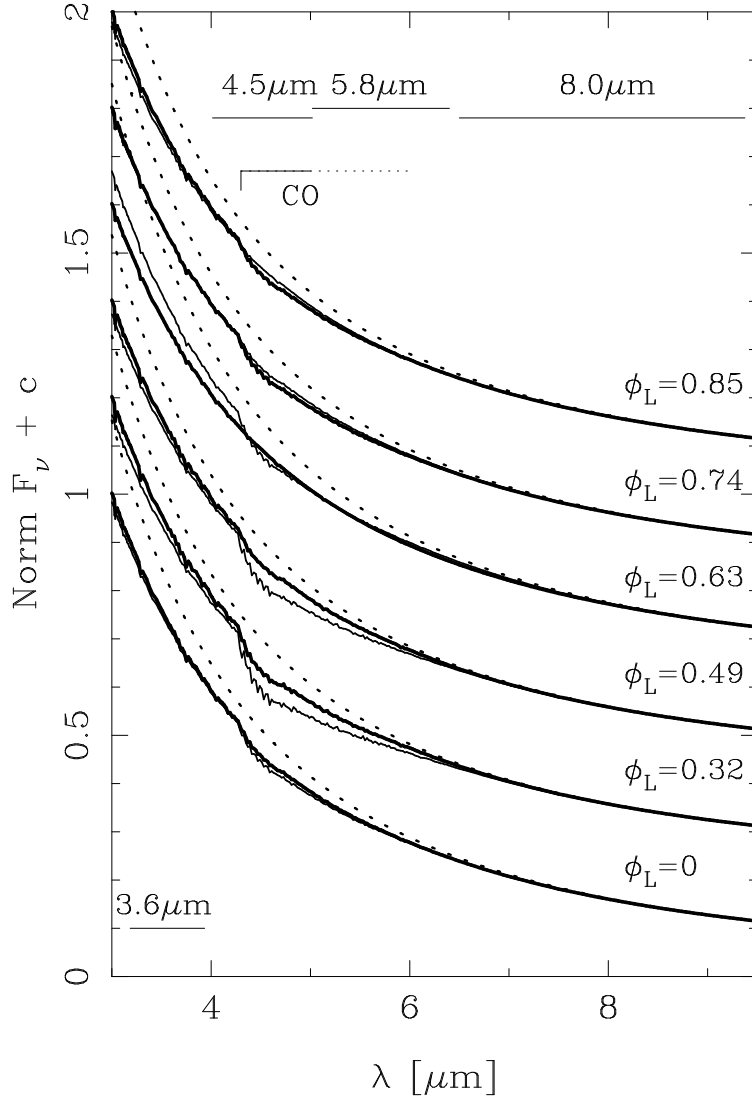


Fig. 6.— Mid-IR model spectra of the 10 d period Cepheid ζ Gem. The thick solid lines are time-dependent hydrodynamic models derived by Marengo et al. (2002). The thin solid lines are instead equivalent models having the same T_{eff} and $\log g$ as the dynamic models, but an atmosphere in hydrostatic equilibrium. The dotted lines are Rayleigh-Jeans blackbody fits of the spectra for $\lambda \gtrsim 8 \mu\text{m}$. The spectra are plotted for a number of significant phases: maximum V luminosity ($\phi_L = 0$), maximum radius ($\phi_L = 0.32$), minimum V luminosity ($\phi_L = 0.49$), phase at which a shock-wave is crossing the photosphere ($\phi_L = 0.63$), minimum radius ($\phi_L = 0.74$) and the phase at which the star was observed with IRAC ($\phi_L = 0.85$). A broad CO spectral feature is present at most phases, but with different strength, within the 4.5 and 5.8 μm IRAC pass-bands.

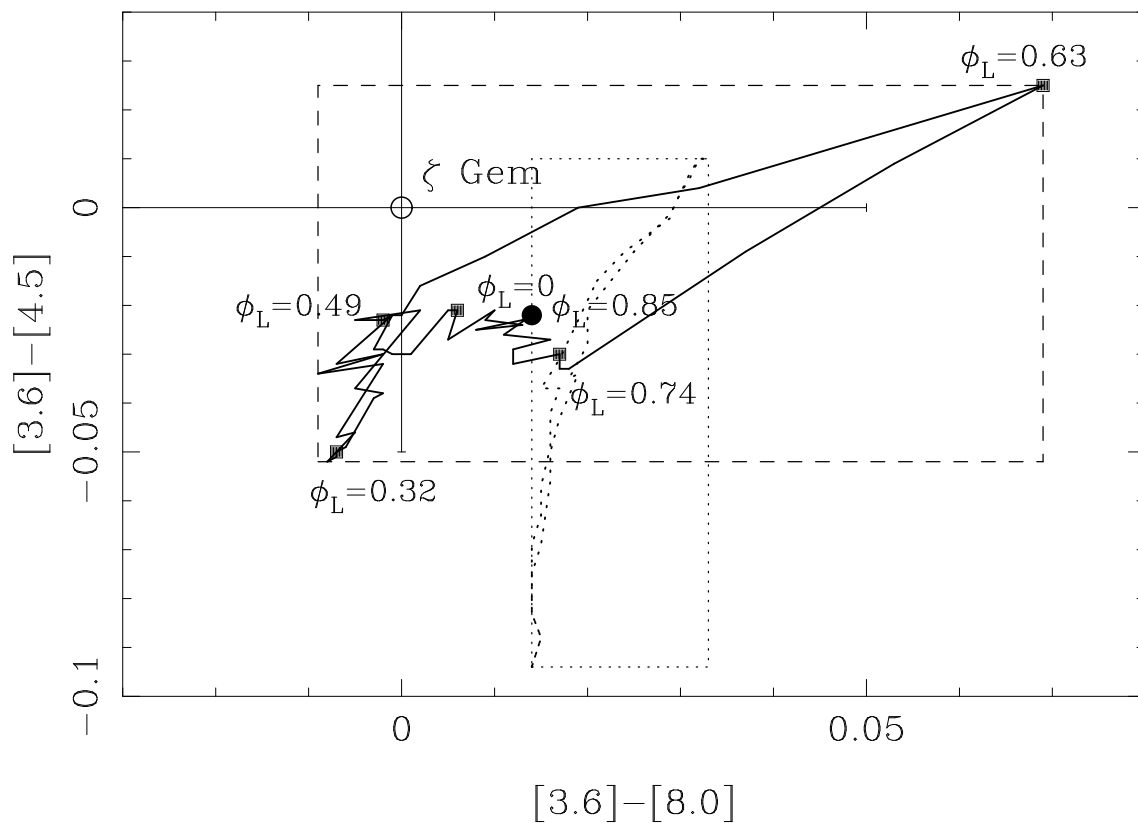


Fig. 7.— IRAC colors of the dynamic (solid line) and static (dotted line) models of ζ Gem. The jitter on the model tracks is due to the finite resolution of the T_{eff} and $\log g$ model grid. The colors of the dynamic model at the same phases of the spectra plotted in Figure 6 are marked (square points). The model and actual colors of the source at the epoch of the IRAC observations are also plotted. The dashed and dotted square boxes indicate the “bounding boxes” of the two class of models (dynamic and static respectively) in the IRAC color space.

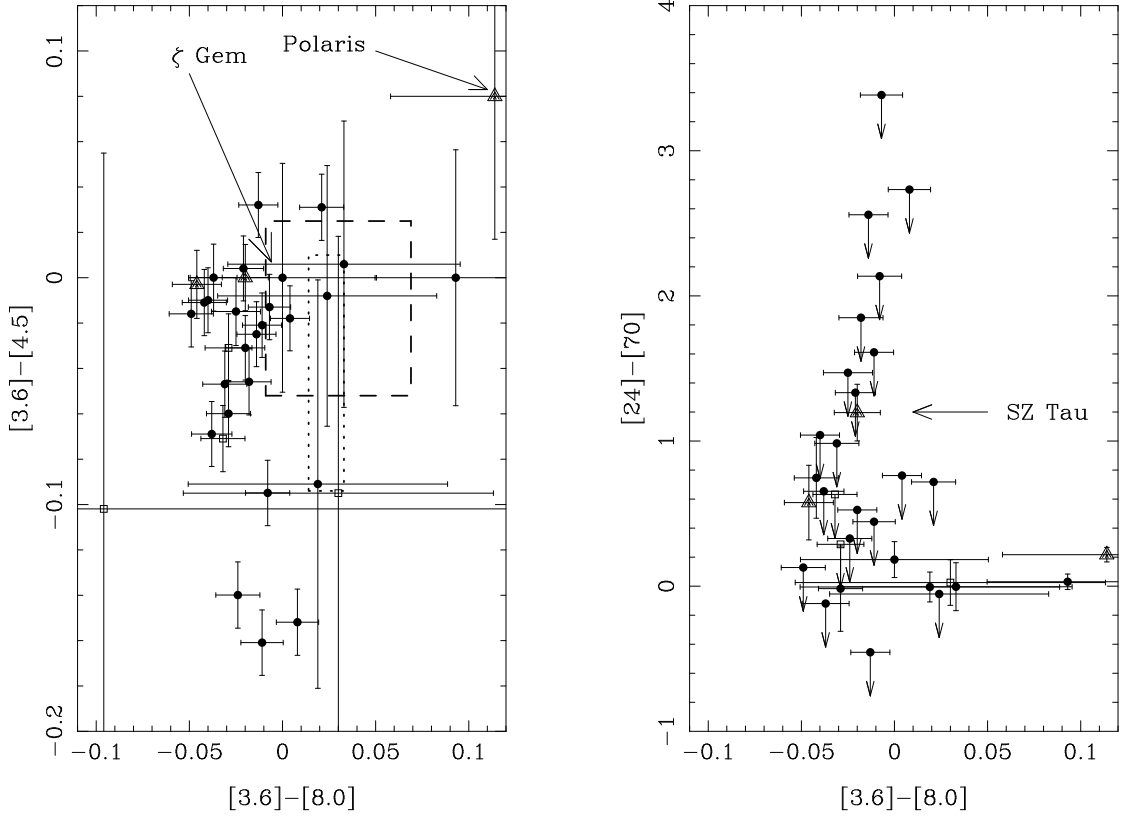


Fig. 8.— Color-color diagrams of our sample. *Left panel* — IRAC $[3.6] - [8.0]$ vs. $[3.6] - [4.5]$ colors. The $[3.6] - [8.0]$ color shows a small spread (~ 0.05 mag) for most of the sources. The $[3.6] - [4.5]$ color has instead a much larger spread, well above the variations allowed by the photometric uncertainties. Polaris is the source with redder colors (~ 0.1 mag). The dashed and dotted boxes indicate the location of the ζ Gem dynamic and static models, respectively. *Right panel* — IRAC $[3.6] - [8.0]$ vs. MIPS $[24] - [70]$ color: only one source (SZ Tau, triangle indicated by arrow) has a statistically significant excess in the $[24] - [70]$ color. Other sources seem to be on a sequence of increasing colors, but the trend may be a spurious artifact, due to the absence of reliable $70 \mu\text{m}$ detections. The 3 supergiants and the red giant in our sample (square symbols) have indistinguishable colors from those of the Cepheid stars, in both diagrams.